

1 **Thermoresponsive Stiffness Softening of Hierarchically**
2 **Porous Nanohybrid Membranes Promotes Niches for**
3 **Mesenchymal Stem Cell Differentiation**

4 Linxiao Wu¹, Adrián Magaz^{1,†}, Arnold Darbyshire¹, Ashley Howkins², Alan Reynolds²,
5 Ian W. Boyd², Hang Song³, Jin-Hua Song³, Marilena Loizidou¹, Mark Emberton¹,
6 Martin Birchall⁴, Wenhui Song^{1*}

7
8 ¹Centre for Biomaterials in Surgical Reconstruction and Regeneration, Division of
9 Surgery & Interventional Science, University College London, London, United
10 Kingdom

11 ²Institute of Materials and Manufacturing, Brunel University London, London, United
12 Kingdom

13 ³School of Innovation and Entrepreneurship, Department of Materials Science and
14 Engineering, Southern University of Science and Technology, Shenzhen, China

15 ⁴UCL Ear Institute, Royal National Throat, Nose and Ear Hospital, University College
16 London, London, United Kingdom

17 † Current address: Bio-Active Materials Group, School of Materials, The University of
18 Manchester, Manchester, United Kingdom

19
20 *Corresponding author, e-mail: w.song@ucl.ac.uk

21 **Abstract**

22 Despite the attention given to the development of novel responsive implants for
23 regenerative medicine applications, the lack of integration with the surrounding tissues
24 and the mismatch with the dynamic mechanobiological nature of native soft tissues
25 remain in the current products. Hierarchical porous membranes based on a poly (urea-
26 urethane) (PUU) nanohybrid have been fabricated by thermally-induced phase
27 separation (TIPS) of the polymer solution at different temperatures. Thermoresponsive
28 stiffness softening of the membranes through phase transition from the semicrystalline
29 phase to rubber phase and reverse self-assembling of the quasi-random nanophase
30 structure was characterized at body temperature near the melting point of the crystalline
31 domains of soft segments. The effects of the porous structure and stiffness softening on
32 proliferation and differentiation of human bone-marrow mesenchymal stem cells (hBM-

33 MSCs) were investigated. The results of immunohistochemistry, histological, ELISA
34 and qRT-PCR demonstrated that hBM-MSCs maintained their lineage commitment
35 during stiffness relaxation; chondrogenic differentiation was favored on the soft and
36 porous scaffold, while osteogenic differentiation was more prominent on the initial stiff
37 one. Stiffness relaxation stimulated more osteogenic activity than chondrogenesis, the
38 latter being more influenced by the synergetic coupling effect of softness and porosity.

39 **Keywords**

40 Stiffness softening, porosity, nanohybrid elastomer, hBM-MSCs, osteogenesis,
41 chondrogenesis

42 **1. Introduction**

43 Native tissues are dynamic systems with changing physico-chemical properties that
44 continuously remodel throughout life, with the cell microenvironment shifting through
45 tissue homeostasis, development, healing or disease progression. Conventional 3D
46 systems, either used as implants/scaffolds in tissue engineering or as cell culture
47 platforms in fundamental cell biology, possess stable static stiffness and cannot capture
48 the dynamics of the extracellular matrix (ECM),^[1] lacking the changing biological
49 elastic nature required in several cellular processes.^[2] Furthermore, current products are
50 intentionally made with much stronger and stiffer properties than actual needs. In fact,
51 the high stiffness and lacking such dynamic biological nature contribute to the
52 mechanical mismatch between a scaffold or implant and the host tissue, which
53 determines the severity of bone weakening, the so-called stress shielding effect, or soft
54 tissue stiffening due to fibrosis encapsulation.^[3,4] These result in non-directed
55 organization and misalignment of collagen fibers that reduce the physiological load-
56 bearing capacity of the newly formed tissue, which leads to poor tissue regeneration or
57 integration, and eventually, implant loosening or organ failure.^[5-7]

58 There has been a growing interest in recent years in developing ‘stimuli-responsive’ or
59 ‘smart’ scaffolds/implants that can mimic the dynamic viscoelastic nature of native
60 tissues.^[1,8,9] On the other hand, the understanding of mechanotransduction, e.g. how
61 cells and tissues recognize and respond to various physico-chemical and mechanical
62 stimuli, is still a major challenge due to the inaccessible real-time tests of live-cells and
63 tissues *in vivo* and the lack of dynamically tunable matrices as *in vitro* models.^[8] The
64 recent development of dynamic cell culture platforms have proved invaluable to

65 improve the understanding of the roles of biochemical and physico-mechanical cues in
66 stimulating and modulating cellular responses.^[8]

67 Dynamic stress conditions^[10] such as mechanical loadings with varying intensity or
68 frequency are known to promote bone and cartilage tissue development. Most *in vitro*
69 research focuses on the impact of the material stiffness on differentiation of stem
70 cells,^[11–14] cellular adhesion and proliferation,^[15] and motility of contractile cells.^[16,17]

71 In recent years, an increasing number of studies have shown that dynamic changes in
72 the substrate stiffness significantly influence cell differentiation processes. For instance,
73 mesenchymal stem cells (MSCs) were seeded on soft magnetoactive hydrogels whose
74 matrix elasticity was modulated by a magnetic field.^[18] Results showed that dynamic
75 stiffening at late time points increased cell spreading and cytoskeleton tension, which in
76 turn boosted the secretion of proangiogenic molecules and the propensity to undergo
77 osteogenesis. The influence on the cell area was reversible and reduced with the
78 removal of the magnetic field. A variety of hydrogel systems, whose matrix stiffness can
79 be regulated by means of an applied stimulus ^[8,19–28] have been developed in recent
80 years to study various cellular behaviors. Despite appealing biocompatibility, the range
81 of stiffness achieved by modifying a hydrogel crosslinking degree is limited,^[29] which
82 may not be strong and stiff enough for cartilage and bone tissue regeneration.
83 Controlling chemical crosslinking degree of the hydrogels has been often used to tune
84 the stiffness, thus, a coupling effect of stiffness hardening and molecular chemical
85 structure are unavoidable in most of hydrogel models reported.

86 The spatio-temporal control of mechanobiological factors regulating the interplay
87 between cells and the ECM has also received great attention to improve the fundamental
88 understanding of cell mechanobiology in the fields of tissue engineering and
89 regenerative medicine.^[1] Well-controlled spacing, shape and pattern of 2D
90 nanotopographic surfaces have been reported to regulate the balance of osteogenic and
91 adipogenic differentiation of hMSC.^[30] It has also become evident that one pore size can
92 be good for a specific cell type but not necessarily optimal for another within the same
93 scaffold type.^[31,32] 3D scaffolds and stimuli-responsive 4D scaffolds show more
94 potential for mimicking true biological microenvironment for tissue/organ
95 regeneration.^[9] Their microarchitecture has been widely investigated on modulating
96 cell-material interactions, influencing the initial cell attachment and migration
97 processes,^[33–35] and on subsequent cellular differentiation.^[30,36] For instance, MSC

98 differentiation towards the chondrogenic lineage has been shown to be mediated by the
99 average pore size of a collagen scaffold, with significantly higher proliferation and more
100 cartilage-like matrix deposition on membranes with relatively higher micro- pore sizes
101 (i.e. 300 μm) compared to those with smaller mean micro- pores (i.e. 94-130 μm).^[36]

102 While there are several methods available to prepare scalable micro/nano- porous
103 membranes or 3D porous scaffolds,^[37] gas foaming, freeze drying, phase separation (or
104 coagulation), particulate leaching, thermally-induced phase separation (TIPS) and 3D
105 printing have been widely used over the years. Gas foaming^[38] permits good
106 interconnectivity of the pores but requires from the use of highly viscous solutions or
107 foaming agents that may impact the biological response of the scaffold. Freeze-drying,
108 phase separation (or coagulation) and particulate leaching,^[39,40] often used to fabricate
109 porous membranes, can control the pore size to a certain extent; however, they can
110 result in non-uniform porous structures, limited interconnectivity, isolated pores or
111 tightly close geometric packing, which in turns can affect the cellular-scaffold
112 interactions. TIPS, on the other hand, can offer improved control over the pore size,
113 pore morphology, and pore interconnectivity by varying the processing conditions.^[41,42]
114 The TIPS process has been recently further developed to 3D-TIPS in combination with
115 3D printing, which has up-scaled the conventional TIPS to overcome the limitations of
116 manufacturing constructs with thick walls and complex geometries, a wider hierarchy of
117 uniform pore structure as well as connectivity.^[43]

118 A family of non-degradable scaffolds based on poly (urea-urethane) (PUU) nanohybrids
119 terminated by polyhedral oligomeric silsesquioxane (PUU-POSS) produced by 3D-
120 TIPS showed stiffness softening at body temperature. ^[43] These 3D-TIPS constructs
121 were found to promote cellular proliferation of dermal fibroblasts ^[43]and differentiation
122 of mesenchymal stem cells *in vitro*,^[44] and guide vascularization and modulate
123 macrophage polarization *in vivo*.^[45] The hyperelasticity, promotion and regulation of
124 chondrogenesis and osteogenesis of MSCs on PUU-POSS scaffolds by 3D-TIPS show
125 promise for repair and regeneration of cartilage and its interface with bone. To
126 understand the nature of phase separation and microphase separation of PUU
127 nanohybrids during TIPS process without the confinement of digitally printed macro-
128 porous networks by 3D-TIPS, herein the unique porous structure, tunable tensile
129 mechanical properties and stiffness softening of PUU nanohybrid membranes
130 manufactured by various TIPS processing conditions are systematically studied and

131 characterized. The effects of their stiffness softening, surface morphology and
132 micro/nano- porosity of the membranes on chondrogenic and osteogenic differentiation
133 of human bone-marrow mesenchymal stromal cells (hBM-MSCs) are revealed.

134 **2. Results and Discussion**

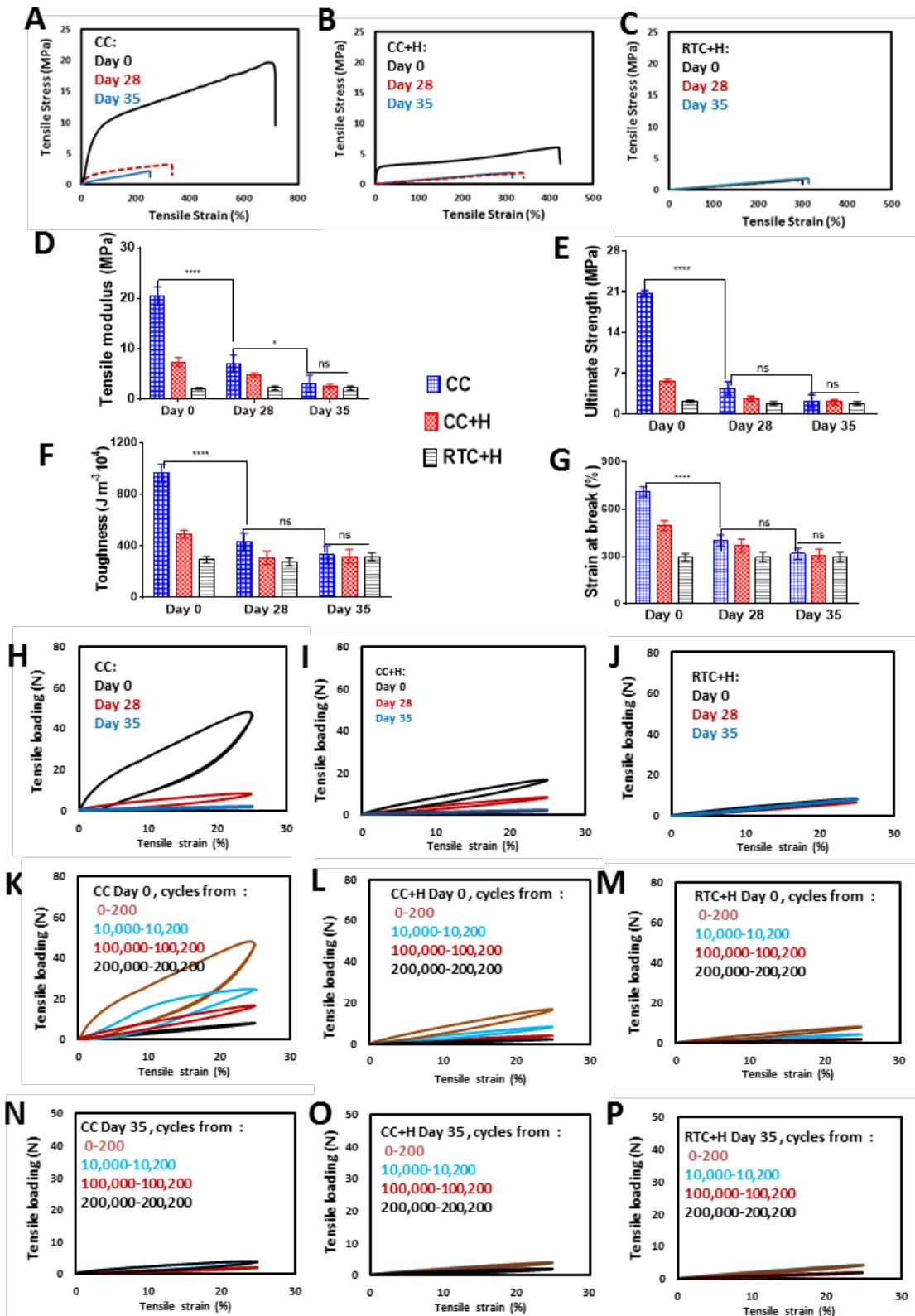
135 Elastomer membranes of PUU with chain ends terminated with POSS nanocage were
136 fabricated following a TIPS process on a flat glass mold. Three different thermal
137 processing conditions were developed in parallel to an inversely 3D printed protocol
138 reported recently ^[43] as comparison, summarized in **Table 1** in Methods, rendering
139 membranes with differential starting stiffness and porous structure. Three different
140 scaffold groups were developed: cryo-coagulation (CC), cryo-coagulation and heating
141 (CC+H), and room temperature coagulation and heating (RTC+H).

142 **2.1 Tunable stiffness softening with hierarchical porous structures by TIPS**

143 The membranes made at the three phase separation conditions behaved differently under
144 tensile stress (**Figure 1**). Despite the highest porosity (89%), CC membranes possessed
145 outstanding hyperelastic mechanical behavior with the highest tensile modulus (20.0
146 MPa), strength (20.7 MPa), ultimate strain (711%) and toughness ($767 \text{ J. m}^{-3} \times 10^4$),
147 compared with CC+H and RTC+H (**Figure 1A-C, Table S1**). Similar to the membranes
148 made by reverse 3D printing,^[43] pronounced stiffness relaxation was also observed in
149 the CC group at body temperature (37°C) (**Figure 1D-G, Table S1**). After a 28-day
150 period of isothermal relaxation, a decrease in all mechanical properties (**Figure 1A-G**)
151 was exhibited, especially within the CC scaffold group, with a significant reduction of
152 the tensile modulus (62%) and strength (82%) respectively ($p < 0.001$); after 35 days
153 incubation, all groups reached similar values (p -value non-significant), reminiscent of
154 their ‘stiffness memory’ effect in 3D-TIPS scaffolds.^[43] It is of note that, after stiffness
155 softening, the tensile moduli of all the TIPS membranes reduced to about 2-3 MPa
156 (**Figure 1D and Table S1**), which is in the similar level of cartilage, higher than those of
157 3D-TIPS scaffolds with additional larger macro-pores introduced by 3D printing (0.3 to
158 1.0 MPa).^[43]

159 The stiffness softening was accelerated at dynamic cyclic tensile loadings (i.e. 200
160 cycles) with a fixed strain at 25% before and after isothermal relaxation up to 35 days
161 (**Figure 1H-J, Table S2**). While it was evident that both the CC and CC+H membranes
162 became softer with increasing reversible compliance, the RTC+H group did not exhibit

163 too much change. The continuous softening and memory of the hyperelastic rubber
164 phase were tracked when subjected to high cyclic numbers up to 2×10^6 times at 37°C
165 (**Figure 1K-M**). As the number of cycles increased, the pronounced damping and
166 reduction of the load amplitude and hysteresis loop area were evident in all samples of
167 CC membranes, and a small trace of stiffness relaxation in CC+H was also detected,
168 compared to RTC+H (**Table S2**). A wider spectrum of relaxation times was associated
169 with the CC group compared to the rest of the sample groups. After 35 days, all
170 membranes relaxed to similar hyperelasticity, showing reversible and linear stress and
171 strain profiles with little hysteresis energy loss measured throughout the prolonged
172 cycles, confirming the ‘stiffness memory’ effect of the membranes (**Figure 1N-P**).

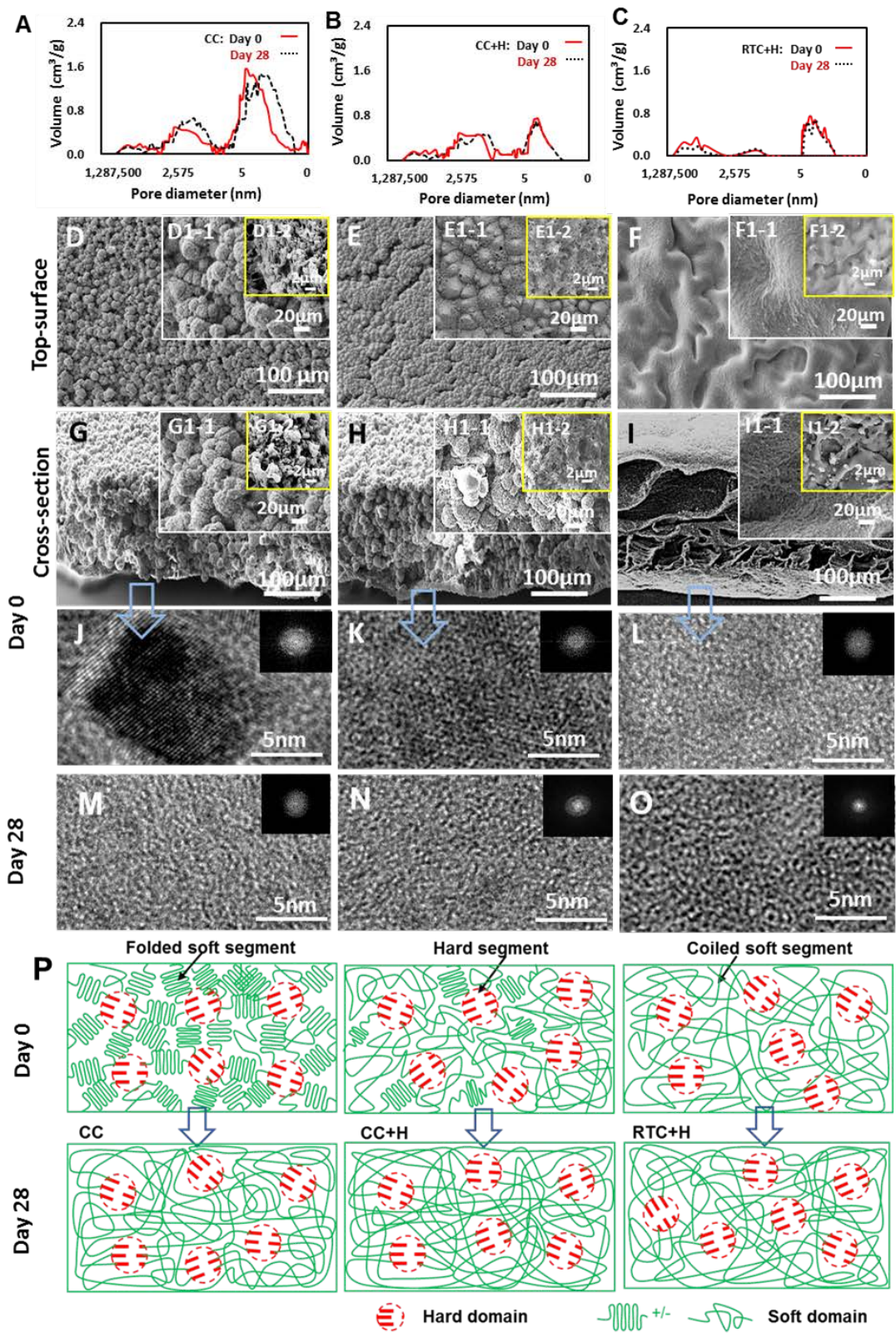


173

174 **Figure 1** Stiffness softening produced by TIPS at three processing conditions (CC,
 175 CC+H and RTC+H). (A-C) Representative stress-strain curves. (D-G) Tensile
 176 mechanical properties before and after incubation >35 days at 37°C for tensile modulus,

177 ultimate tensile strength, toughness and strain at break (n=6). (H-J) Dynamic cyclic
178 tensile loading at 0-200 cycles before and after 35 days (n=2); (K-M) dynamic tensile
179 loading at increasing cycles at day 0 (n=2); (N-P) dynamic tensile loading at increasing
180 cycles at day 35 (n=2). The differences between the experimental groups were analyzed
181 by two-way ANOVA with Tukey's post hoc test, or two-tailed unpaired Student's t test.
182 ****p<0.0001; *p<0.05; n.s = non-significance.

183 All scaffold groups exhibited a hierarchical porous structure spanning a wide range of
184 scales from macro-, micro- to nanometers (300 μm to 0.1 nm), but with different size
185 distributions. The average pore diameter and pore size distribution of the three different
186 scaffold groups were compared by mercury intrusion porosimetry (**Figure 2A-C, Table**
187 **S3**) and electron microscopy (SEM) (**Figure 2D-I**). The CC scaffold exhibited the
188 widest hierarchy of pore size distribution but with predominant micro- to nano- pores
189 (84% of pore size <10 μm), hence the overall highest porosity (89%) and surface area
190 (160.86 $\text{m}^2\cdot\text{g}^{-1}$) (**Figure 2A, Table S3**) as a result of a slow coagulation at the liquid-
191 solid interface between water and the frozen polymer solution. There was a slight
192 shrinkage (82% porosity and 155.78 $\text{m}^2\cdot\text{g}^{-1}$ surface area) after incubation for 28 days at
193 37°C. This is further supported by the relatively uniform porous bead-like morphology
194 from the top surface throughout the whole cross-section in CC membranes due to the
195 cryo-process, as seen under SEM at different magnifications (**Figure 2D, G**). The
196 CC+H scaffold presented a slightly smaller porosity (80%) to that of CC with some
197 decrease of the pores at the micro- and nano- scales (80% pores <10 μm), and thus
198 surface area (128.17 $\text{m}^2\cdot\text{g}^{-1}$) (**Figure 2B, Table S3**) due to shrinkage resulting from the
199 post-thermal treatment. Those beads appeared to be fused with less nano- pores due to
200 the shrinkage (**Figure 2E, H**). The RTC+H group exhibited the lowest porosity (71%)
201 with a significant reduction of pores at micro/nano- meters (only 49% pores <10 μm),
202 thus the lowest pore surface area (49.92 $\text{m}^2\cdot\text{g}^{-1}$) (**Figure 2C, Table S3**). A dense skin-
203 like surface of the membrane was generated at the liquid-liquid interface between water
204 and the polymer solution and non-uniform macro- pores under skin across the whole
205 thickness of the membrane were produced by a faster coagulation at room temperature
206 (**Figure 2F, I**).



207

208 **Figure 2 Hierarchical structure of ‘stiffness memory’ PUU-POSS membranes by**
 209 **TIPS at various phase separation conditions (CC, CC+H and RTC+H), before and**
 210 **after 28 days incubation *in vitro* at body temperature. (A-C) Pore size and size**
 211 **distribution. (D-I) SEM micrographs demonstrating morphology and porous structure at**

212 the (D-F) top-surface and (G-I) cross-section. (J-O) HRTEM images of the membranes
213 at day 0 (J-L) and after 28 days (M-O) *in vitro* incubation (insets of electron
214 diffractions). (P) Schematic of phase transition of the nanophase structure before and
215 after stiffness softening of the membranes *in vitro*.

216 XRD spectra (**Figure S1 A-C, Table S4**) and high resolution TEM (**Figure 2J-O**) shed
217 more insight on the stiffness softening mechanism. The phase transition from
218 semicrystalline domain to amorphous rubbery soft domain is the driving force for
219 stiffness softening. HRTEM images (**Figure 2J-O**) verified the phase transition and
220 evolution of the nanophase structure of these membranes before and after incubation for
221 28 days, in consistence with WAXD spectra (**Figure S1 A-C**). The bright crystalline
222 nano-domain of soft segments organized the dark nano-domains of hard segments into a
223 highly ordered nanophase structure in as-produced CC membranes (**Figure 2J**), which
224 contributed to the overall high mechanical properties (**Figure 1**). Such ordered structure
225 gradually disorganized into a random nanophase structure of soft and hard segments,
226 with evidence of a diffusion halo from both electron diffraction (**Figure 2M**) and
227 WAXD (**Figure S1 A**) after incubation for 28 days, resulting in stiffness relaxation
228 observed in **Figure 1**. **Figure 2K** showed a mesophase-like stage of melting crystalline
229 nanophase structure of CC+H membranes after 3 h of thermal treatment at 40°C.
230 RTC+H membranes formed a uniform rubber nanophase structure with hard domains as
231 physical crosslinking points randomly distributed into a continuous soft domain, a
232 typical nanophase structure of thermoplastic polyurethanes (**Figure 2L**), showing
233 characteristics of hyperelasticity of the elastomer. After incubation for 28 days, all the
234 membranes shared a more or less similar random nanophase structure as shown in
235 **Figures 2M-O**. Besides, there was a subtle change in the rubber nanophase structure
236 over the time of incubation as indicated by WAXD spectra, with emerging three
237 pronounce broad halo peaks with 2θ at around 20°, 29° and 41° (**Table S4**), suggesting
238 the low-dimensional and short distance chain packing of hard and soft chain segments
239 and their interface during the incubation. Therefore, such nanophase structure is not
240 completely random, named quasi-random nanophase. The phase transition and
241 subsequent reverse self-assembling during stiffness softening echoed a wider spectrum
242 of relaxation times associated with the CC group compared to the other two sample
243 groups, which was revealed by the dynamic mechanical test above.

244 Like other polyurethane elastomers, PUU-POSS is chemically stable and non-

245 degradable. It is clear that the differences in the measured stiffness (**Figure 1 D-G** and
246 **H-P**) and corresponding phase structures (**Figure 2D-I and J-O**) of the membranes at
247 different processing conditions, incubation and cyclic loading over the time at body
248 temperature, are contributed by the polymer chain organization and interaction at
249 multiscale. This physical evolution of condensed structure of PUU-POSS elastomer
250 involves chain conformation, nano- phase separation, and phase transition between the
251 semicrystalline phase and quasi-random rubber phase, during the crystallization/melting
252 of the soft segments and self-assembly/inverse self-assembly of both soft and hard
253 segments.^[43,45] Besides, the stiffness softening effect (**Figure 1P**) could be in principle
254 reversible or partially reversible by re-crystallization or densely packing at a suitable
255 temperature; however, it may be kinetically slow in the solid state.

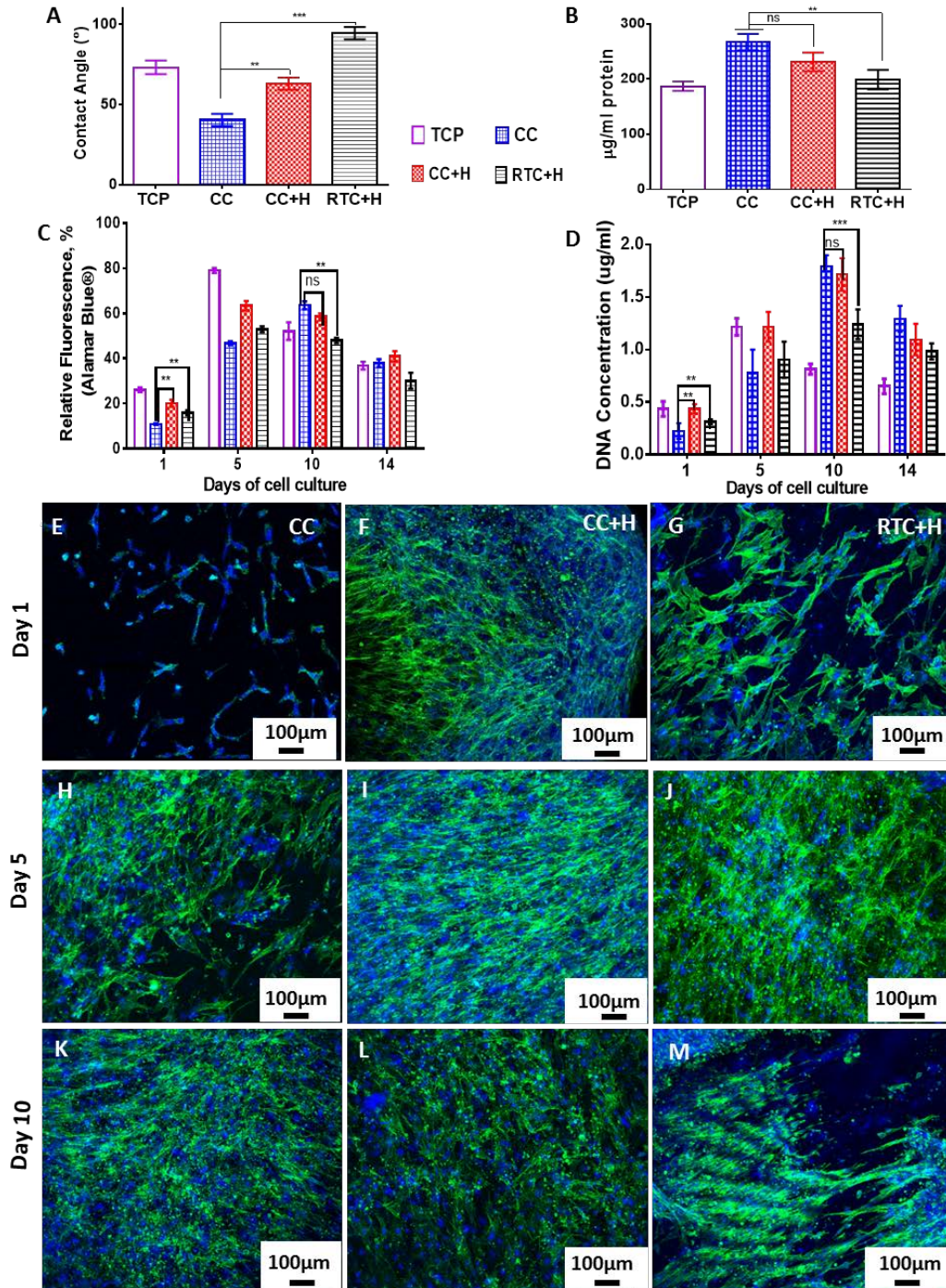
256 **2.2 Effects of porosity and stiffness softening on hBM-MSCs proliferation**

257 The surface wettability (**Figure 3A**) and protein adsorption (**Figure 3B**) of the scaffold
258 groups were characterized. The CC group demonstrated the lowest contact angle and
259 highest protein adsorption compared to CC+H and RTC+H, which is attributed to its
260 unique surface porous structures at the micro- and nano- scales (**Figure 2D, G**). Despite
261 the hydrophobic nature of PUU-POSS nanohybrid elastomer, the uniform micro- to
262 nano- porous structure formed at the surface of the CC group acted as a capillary,^[46]
263 which absorbed water, thus, increasing the wettability of the surface and protein
264 adsorption. Similar capillary effects took place on CC+H to a lesser extent due to the
265 small shrinkage after the post treatment (**Figure 2B** and **Table S3**). In contrast, the
266 RTC+H group showed the highest contact angle and lowest protein adsorption
267 contributed by the formation of the dense surface.

268 Cells exhibited higher metabolic activity and proliferation rates on the initially soft
269 CC+H scaffold at day one post-seeding, but a significant peak ($p < 0.01$) was reached at
270 day 10 on the CC scaffold. Although non-significant differences were found after a 10-
271 day period between the CC and CC+H group (**Figure 3C-D**), cell proliferation was
272 accelerated on CC scaffolds where stiffness softening was taking place, while remaining
273 significantly higher than the RTC+H group until confluence ($p < 0.01$). This trend of
274 cellular viability was also visualized by fluorescent phalloidin F-actin staining under
275 confocal microscopy (**Figure 3E-M**). A distinct difference of cell morphology on the
276 three membranes were observed at the early stages of cell culture, with the most number

277 of MSCs and filamentous actin (F-actin, in green) on CC+H samples and the least on
278 the CC ones (**Figure 3 E-G**), in agreement with the results of metabolic activity and
279 total DNA (**Figure 3C-D**). In combination with the morphology of cells via SEM at day
280 5 (**Figure S2**), more insight is shed that cell bodies were flat on all three scaffolds but
281 with more long actin spindles on soft membranes of CC+H and RT+H despite distinctly
282 different surface topology. This indicates that the soft surface of CC+H and RT+H
283 promoted more expression of filopodium/lamellipodium that enhanced cell adhesion
284 and migration on the membrane.

285 On the other hand, MSCs appeared to migrate and proliferate slowly on the stiff surface
286 of CC samples in the early stage of the cell culture (**Figure 3E** and **Figure S2**) despite
287 their most hydrophilic surface and highest protein absorption among the three groups
288 (**Figure 3A-B**). Nevertheless, the profound stiffness relaxation effect exhibited by CC
289 samples (**Figure 1 D-G**) during the first 2 weeks of incubation ^[43] appeared to trigger
290 more cellular metabolic activity and accelerated proliferation for a relative longer period
291 of time, coupled with a greater hierarchical micro/nano- porous structure (**Figure 2D,**
292 **G**). The highest cellular viability and substantial cellular reorganization on the CC
293 membranes over 10 days while stiffness softening was occurring was confirmed by
294 confocal microscopy (**Figure 3K**).



295

296 **Figure 3 HBM-MSC proliferation on stiffness softening porous membranes by**
 297 **TIPS at various thermal conditions (CC, CC+H and RTC+H): (A-B) Wettability**
 298 **(n=3) and protein adsorption (n=3); (C-D) metabolic activity and cellular proliferation**
 299 **(n=3); (E-M) Immunofluorescent staining (F-actin in green and nuclei in blue) over 10**
 300 **days. The differences between the experimental groups were analyzed by two-way**
 301 **ANOVA with Tukey's post hoc test. **p<0.01, *** p<0.001; n.s = non-significance.**

302 **2.3 Effects of stiffness softening and porosity on *in vitro* chondrogenesis of hBM-**
303 **MSCs**

304 Chondrocyte-like MSCs were highly present on the CC+H and CC membranes (**Figure**
305 **4A-B**), highlighted by Collagen II and Aggrecan markers under a fluorescent confocal
306 microscope at day 28 of chondrogenic differentiation, in contrast to RTC+H (**Figure**
307 **4C**). SOX 9, an important regulator of the chondrocyte phenotype, controls gene
308 expression of *COL2A1* (Collagen II), *COLX* (Collagen X) and *ACCAN* (Aggrecan), all
309 of which encode important cartilage-like extracellular matrix (ECM) proteins ^[47]. More
310 to this point, those gene expression markers of chondrogenesis were quantified by
311 qPCR during differentiation towards the chondrogenic lineage (**Figure 4D-G**). Gene
312 expression activity increased with the culture time in all scaffold groups to different
313 extents, compared to tissue culture plate (TCP) control. Among the various scaffold
314 groups, the CC+H scaffold appeared to promote the highest expression of all
315 chondrogenic markers throughout the 28 days of differentiation. The relative gene
316 expression of *ACCAN*, *SOX9*, *COL2A1* and *COLX* in the CC+H scaffold was
317 significantly higher ($p < 0.001$) than the spheroid positive control after 4 weeks of
318 culture. The levels of sulfated glycosaminoglycans (sGAG) per DNA content
319 (sGAG/DNA) were also the highest for the CC+H group among the rest of the scaffold
320 groups ($p < 0.01$) (**Figure 4H**). It is of note that the gene expression values quantified for
321 the stiffer CC group with similar surface and porosity were lower than those for the
322 CC+H group, but still significantly higher than the softer RTC+H group.

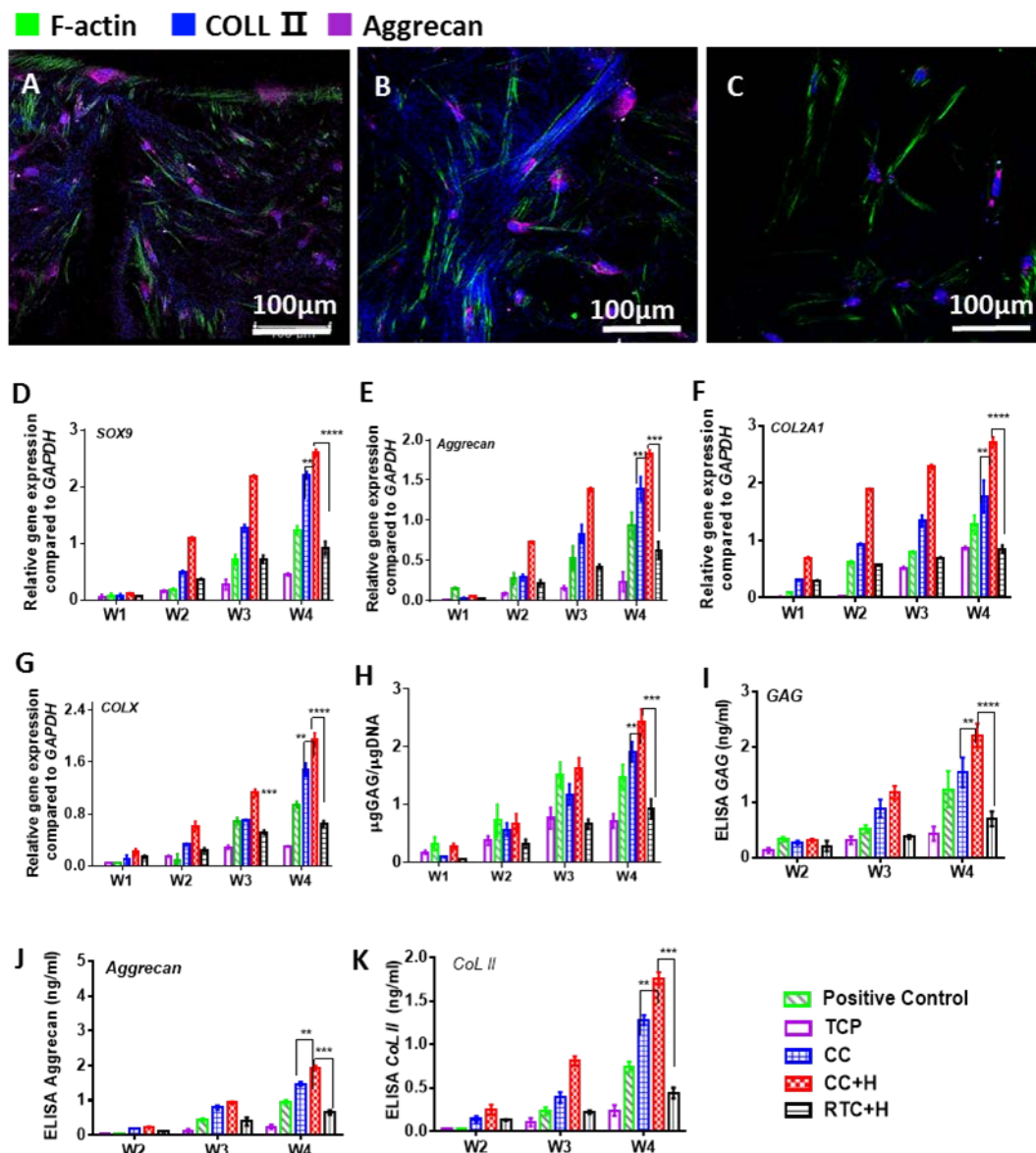
323 An ELISA technique was used to further quantify the production of sGAG, Aggrecan
324 and Collagen II (**Figure 4I-K**). After chondrogenic differentiation, higher expression of
325 glycosaminoglycans, Aggrecan and Collagen II was detected on both CC+H and CC
326 membranes compared to the rest ($p < 0.001$ to 0.01), in consistence with the results
327 obtained by qPCR. This data further confirmed that both the CC+H and CC scaffold
328 groups promoted more rapid chondrogenesis of hBM-MSCs, as demonstrated by
329 histological sectioning at week 4 (**Figure 5**). Increased Collagen II and proteoglycan
330 formation associated with chondrogenesis was observed throughout the whole cross-
331 section of the CC (**Figure 5A1-A4**) and CC+H membranes (**Figure 5B1-B4**). More
332 intriguingly, a large number of MSC cells showing chondrocyte phenotype migrated
333 into the lacunae within the bead-like porous network within the CC and CC+H samples,
334 opposed to those only on the top dense surface of the RTC+H membrane.

335 It was expected that a low distribution of calcium and phosphorous during
336 chondrogenesis was detected by EDX mapping (**Figure 6A, Table S5**). The tensile
337 mechanical properties of the membranes after chondrogenesis differentiation were also
338 compared with cell-free constructs after incubation at 37°C for 35 days (**Figure 6B-E**).
339 Despite the stiffness softening of the CC and CC+H scaffolds themselves, a substantial
340 increase of the resulting stiffness, strength, ultimate strain and toughness respectively
341 was measured, attributed to cell-derived ECM [48,49] into the TIPS-induced porous
342 membranes where most chondrogenesis occurred. The modulus of chondrocyte-like
343 MSC-loaded scaffolds after chondrogenesis reached up to 10 MPa, matched well with
344 stiff native cartilage (2-10 MPa).^[50-54] This is a potentially highly desirable smart
345 cartilage implants/hip implant coatings with high stiffness for providing initial
346 mechanical support and stiffness relaxation for aiding biological tissue remodelling
347 following surgical tissue reconstruction.

348 The CC+H and RTC+H membranes became softer after post thermal treatment, but
349 remained with a distinctly different surface morphology, which indicates the influential
350 role of the surface morphology and hierarchical porous structure of the membranes on
351 regulating chondrogenesis of hBM-MSCs. On the other hand, CC and CC+H
352 membranes, with similar surface morphology and porosity, but different initial stiffness
353 and stiffness softening degree, shed more insight about the cellular responses to the
354 stiffness softening mechanism highly exhibited by the CC samples.

355 **Figures 4-5** show that the MSC fate towards chondrogenesis was mainly favored in
356 terms of the initial soft stiffness of the CC+H scaffold coupled to its hierarchical porous
357 structure. The initial high stiffness of the CC membranes appeared to slowdown
358 chondrogenic differentiation compared to CC+H ($p < 0.01$) in the beginning. As more
359 MSCs grew on the surface and inside of the porous scaffold (**Figure 3**), their
360 differentiation potential was improved and regulated by the ECM derived
361 microenvironment generated by earlier differentiated cells on the substrate with on-
362 going stiffness softening, a similar trend to the MSCs on reversely 3D-printed scaffolds
363 made by 3D-TIPS.^[44] Therefore, CC membranes remained efficient chondrogenic
364 differentiation during stiffness softening, significantly higher than RTC+H and both the
365 TCP and positive controls. Histological cross-sections of the cell-laden membranes after
366 differentiation (**Figure 5**) showed that cartilage-like tissue grew and penetrated into the
367 hierarchically micro/nano- porous structures of both CC+H and CC membranes (**Figure**

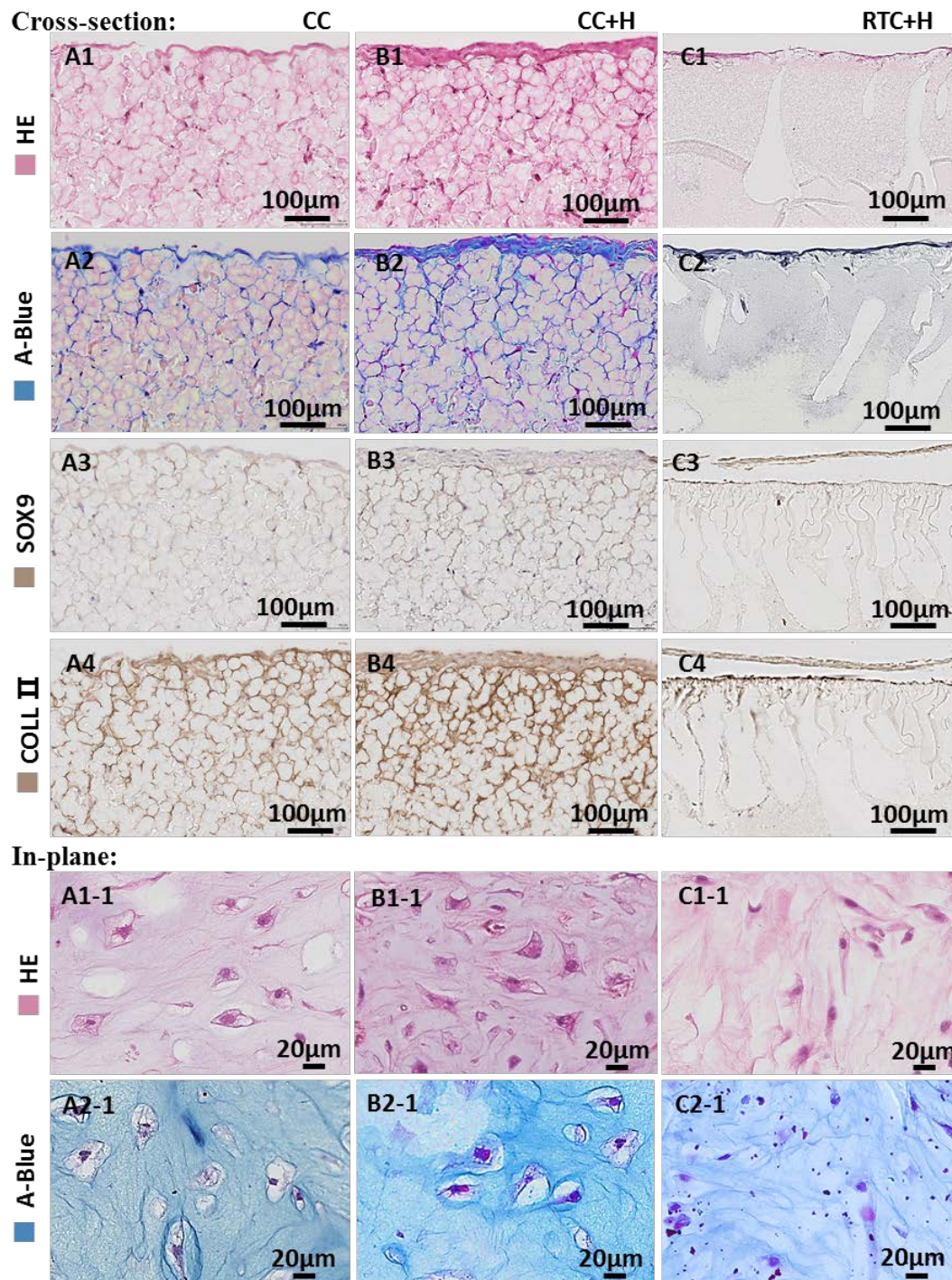
368 **2D-F)** and compared with non cell-laden membrane sections used as negative control
 369 **(Figure S3 A-B)**. Unsurprisingly, only a thin layer of stained tissue was observed on the
 370 surface of the RTC+H scaffold, prone to be delaminated, but very little within the cross-
 371 section due to the low porosity on the dense surface skin **(Figure 2F)**. In short, both CC
 372 and CC+H membranes stimulated more chondrogenesis, thanks to a combination of a
 373 soft matrix or stiffness softening with appropriate hierarchical porosity that allowed
 374 cells to attach, migrate and grow, stimulating cartilage-like integrin mediators and
 375 rendering microenvironment niche for cellular proliferation.



376

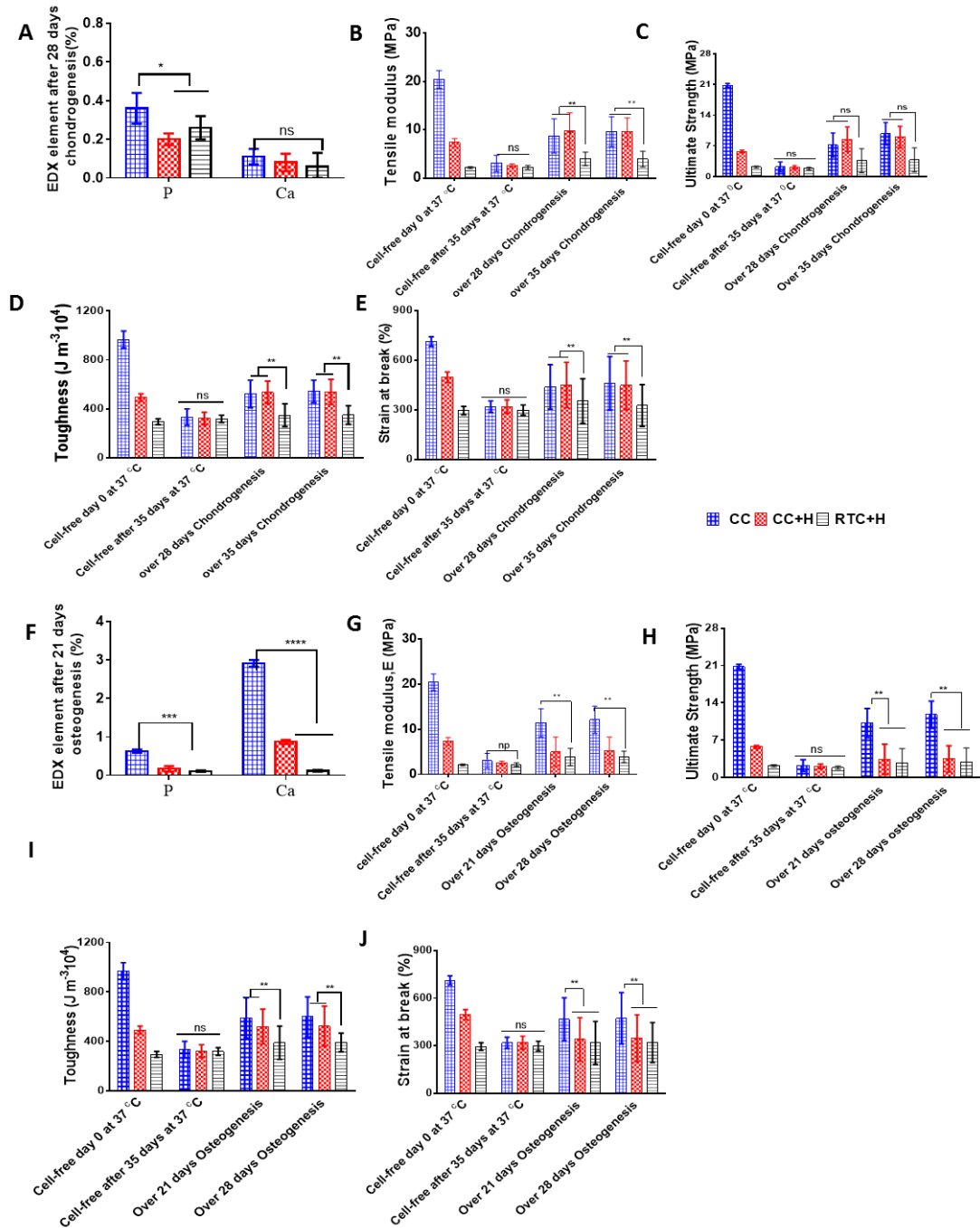
377 **Figure 4 Chondrogenesis of hBM-MSCs on stiffness softening porous membranes**
 378 **(CC, CC+H and RTC+H):** (A-C) Immunofluorescent analysis of hBM-MSC under
 379 chondrogenic differentiation after 28 days showing Collagen II (blue) and Aggreacan

380 (purple), with F-actin (green) counterstaining. (D-G) Gene expression profile by qPCR
 381 over 4 weeks (n=6); comparative analysis for (D) *SOX9*, (E) *ACCAN*, (F) *COL2A1*, and
 382 (G) *COLX*. (H) Synthesis of sulfated glycosaminoglycans during a 4-week period (n=6).
 383 (I-K) ELISA of glycosaminoglycans, Aggrecan and Collagen II production (n=6). The
 384 differences between the experimental groups were analyzed by two-way ANOVA with
 385 Tukey's post hoc test, or two-tailed unpaired Student's t test. **p<0.01; ***p<0.001;
 386 **** p<0.0001.



387

388 **Figure 5 Functional evaluation of chondrogenic differentiation on stiffness**
 389 **softening porous membranes (CC, CC+H and RTC+H):** histological images of the
 390 cross-section ($\times 4$ objective lens) and in-plane ($\times 40$ objective lens) of the membranes at
 391 week 4 stained with Hematoxylin and Eosin, Alcian Blue, SOX9, and Collagen II.



392
 393 **Figure 6 Element detection and tensile mechanical properties of differentiated cell-**
 394 **laden stiffness softening porous membranes.** (A, F) Production of calcium and
 395 phosphorous after chondrogenesis and osteogenesis (n=6). (B-E) Tensile modulus (at
 396 50% strain), ultimate tensile strength, toughness and strain at break after chondrogenic

397 differentiation over 28-35 days compared to day 0 and day 35 after stiffness relaxation
398 of cell-free membranes (n=6). (G-J) Tensile modulus (at 50% strain), ultimate tensile
399 strength, toughness and strain at break after osteogenic differentiation over 21-28 days
400 compared to day 0 and day 35 after stiffness relaxation of cell-free membranes (n=6).
401 The differences between the experimental groups were analyzed by two-way ANOVA
402 with Tukey's post hoc test, or two-tailed unpaired Student's t test. *p<0.05; **p<0.01;
403 ****p<0.0001.

404 **2.4 Effects of stiffness softening and porosity on *in vitro* osteogenesis of hBM-MSCs**

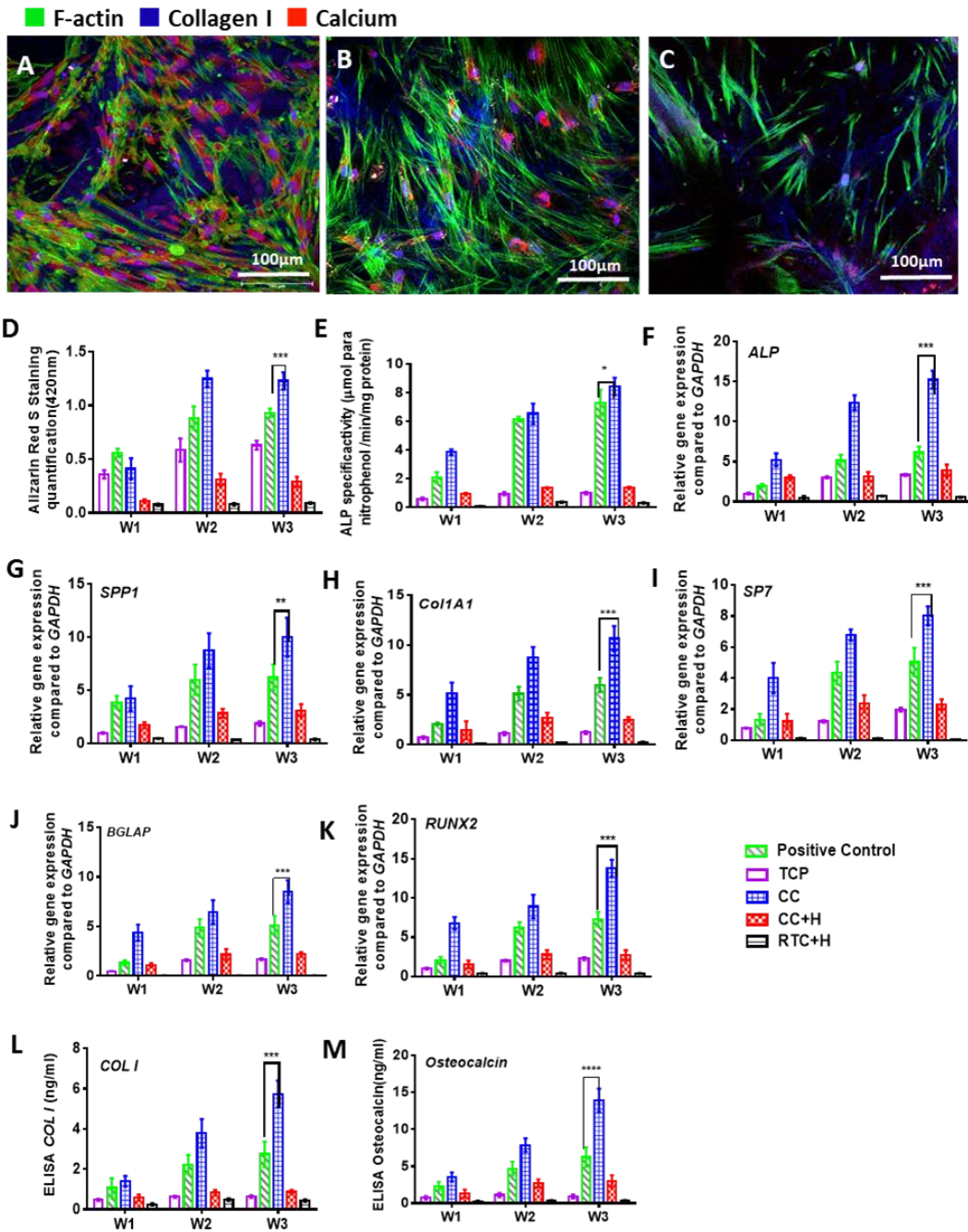
405 The stiffness softening of the membranes also regulated hBM-MSCs towards the
406 osteogenic lineage in the osteogenic differentiation medium. Immunofluorescent images
407 stained by Collagen I and calcium deposition showed that the most osseous tissue
408 formation occurred on the CC membranes after 21 days, opposed to little calcium
409 presence on either the CC+H or RTC+H samples (**Figure 7A-C**). The quantification of
410 osseous tissue formation in terms of Alizarin Red and alkaline phosphatase activity, as
411 markers of calcium deposition, confirmed with significantly higher production on the
412 CC scaffolds compared to both the CC+H and RTC+H groups (p<0.0001) after 3 weeks
413 (**Figure 7D-E**).

414 The gene expression of key regulators of osteogenesis, such as *SP7* (Osterix), *COL1A1*
415 (Collagen I), *SPP1* (Osteopontin), *ALP* (alkaline phosphatase), *BGLAP* (Osteocalcin)
416 and *RUNX2* (cbfa-1) gradually increased during *in vitro* differentiation as evaluated by
417 qPCR (**Figure 7F-K**). Outstanding osteogenic differentiation of hBM-MSCs occurred
418 on the initially rigid CC scaffold within 21 days; with the highest expression of all
419 genes compared to the rest of the membranes and the spheroid positive control
420 (p<0.0001). In addition, the production of Osteocalcin and Collagen I analyzed by
421 ELISA over a 3-week period (**Figure 7L-M**) was significantly higher from the CC
422 membranes than the rest (p<0.0001), in consistence with the results by qPCR.
423 Compared to membranes with 3D digitally printed macro-pores,^[44] such differences are
424 even higher, indicating the stiffness softening as a predominant drive for promoting
425 osteogenesis.

426 Osteogenesis after 21 days on the CC scaffold was also confirmed by the histological
427 staining of Collagen I and Alizarin Red for calcium (**Figure 8**). Deposition of bone-like
428 ECM components associated with osteogenesis was observed predominantly throughout

429 the porous network of the CC scaffold (**Figure 8A1.1, A3.1**), as compared to the
430 negative control (**Figure S3 C**). Calcium deposition on the membranes was also directly
431 detected by EDX analysis (**Figure 6F**), where CC membranes exhibited the highest
432 accumulation (**Table S6**). The tensile mechanical properties of the membranes after
433 osteogenesis were also compared with cell-free constructs after *in vitro* stiffness
434 relaxation > 28 days (**Figure 6G-J**). Similar to the chondrogenesis example, substantial
435 enhancements of all the tensile mechanical properties of the CC group after stiffness
436 softening are attributed to cell-derived produced ECM during the pronounced
437 osteogenesis on the CC group.

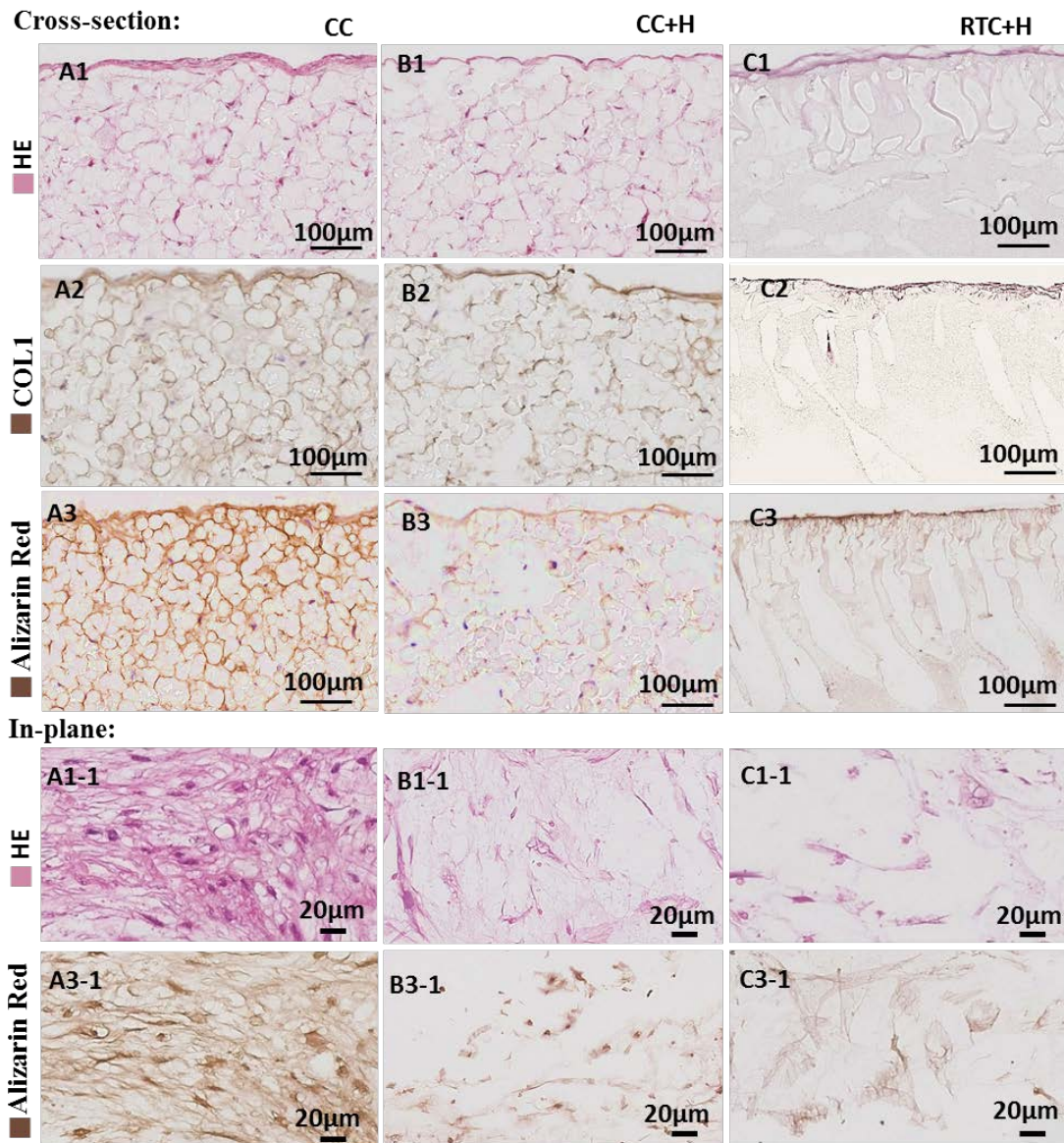
438 Different from the chondrogenesis case studied above, the initial high stiffness and
439 subsequent stiffness relaxation appeared to be predominant factors for promotion of
440 osteogenesis of hBM-MSCs with evidence on the porous CC scaffold. Osteogenesis
441 remained constantly active over the 28-day period (**Figure 7**), regardless the softer
442 substrate after the first two weeks of incubation at body temperature,^[43] indicating the
443 cellular ‘mechanical memory’ of the hBM-MSCs on initial stiff substrates.^[23] Stem cell
444 differentiation is regulated by integrins and an $\alpha 2$ -integrin-ROCK-FAKERK1/2 axis is
445 stimulated on stiff substrates to promote RUNX2 and osteogenesis.^[55] It is therefore
446 postulated that differentiation of MSCs during osteogenesis is modulated by the initial
447 high stiffness of the CC group with enhanced focal adhesion of mediated specific
448 integrins and activated RUNX2 expression leading to bone formation. The proliferation
449 and differentiation of MSCs continued increasing significantly during the subsequent
450 profound stiffness softening of the CC membranes, demonstrating resilient cellular
451 ‘mechanical memory’ regardless the softening substrate. In this case, a gradual shift
452 from the original mechanosensing towards *de novo* cell-derived matrix sensing in a
453 more physiologically microenvironment niche generated by the cells themselves may
454 have occurred. While differences in the associated bone gene expression in the CC+H
455 and RTC+H membranes remained, the effect of the micro/nano- porous structure is
456 again noticeable ($p < 0.05$), but more significant than those in the scaffolds made by 3D-
457 TIPS with digitally printed macro-pores.^[44] Therefore, the influence of the initial
458 stiffness and subsequent stiffness softening of the CC scaffold on modulating
459 osteogenesis is overriding its porosity.



460

461 **Figure 7 Osteogenesis on stiffness softening porous membranes (CC, CC+H and**
 462 **RTC+H).** (A-C) Immunofluorescent analysis of hBM-MSC after 21 days, showing F-
 463 actin (green), Collagen I (blue) and calcium (red). (D-E) Alizarin Red S (n=6) and
 464 alkaline phosphatase activity (n=6) after over 21 days. (F-K) Gene expression profile by
 465 qPCR over 3 weeks (n=6); comparative analysis for (F) *ALP*, (G) *SPP1*, (H) *COL1A1*, (I)
 466 *SP7*, (J) *BGLAP* and (K) *RUNX2*. (L-M) ELISA of Osteocalcin and Collagen I
 467 production (n=6). The differences between the experimental groups were analyzed by
 468 two-way ANOVA with Tukey's post hoc test, or two-tailed unpaired Student's t test.

469 **p<0.01; ***p<0.001.



470

471 **Figure 8 Functional evaluation of osteogenic differentiation on stiffness softening**
472 **porous membranes (CC, CC+H and RTC+H):** histological images of the cross-
473 section ($\times 4$ objective lens) and in-plane ($\times 40$ objective lens) of the membranes stained
474 with Hematoxylin and Eosin, Collagen I and Alizarin Red.

475 3. Conclusion

476 Thermoresponsive elastomer membranes/coatings with a hierarchical micro/nano-
477 porous structure have been developed by TIPS with tunable starting stiffness and
478 stiffness softening at body temperature. The results shed insight on the correlation
479 between the structure and properties of PUU nanohybrid induced from the simultaneous

480 solution phase separation and microphase separation of the PUU nanohybrid during
 481 TIPS and coupling effects of surface morphology, micro/nano- pores and stiffness
 482 softening behavior on modulating stem cell fate. The starting modulus and subsequent
 483 stiffness softening of the membranes are demonstrated to regulate and promote
 484 proliferation as well as osteogenic and chondrogenic differentiation of hBM-MSCs. *In*
 485 *vitro* results show that cartilage-like and bone-forming proteins are synthesized on the
 486 membranes, while hBM-MSCs keep their lineage specification during stiffness
 487 softening, and that proliferation and differentiation processes are accelerated during the
 488 matrix relaxation. The starting high modulus and subsequent stiffness softening of the
 489 porous CC scaffold play a predominant role in promotion of hBM-MSCs osteogenesis.
 490 On the other hand, the coupling effect of a starting low stiffness and micro/nano- porous
 491 structure promotes more efficiently hBM-MSCs chondrogenesis. The thermoresponsive
 492 porous membranes produced here demonstrate potential applications as smart implant
 493 coatings or niche scaffolds for cartilage/bone non-load bearing with matched dynamic
 494 mechanical properties, as well as for valuable dynamic cell culture platforms to further
 495 elucidate the interplay and turnover rate of mechanosensing proteins in response to
 496 changes in the substrate stiffness.

497 **4. Experimental section**

498 **Materials:** Unless otherwise stated, all reagents were purchased from Sigma-Aldrich
 499 (UK).

500 **Fabrication of membranes:** Porous membranes with different stiffness were fabricated
 501 following an adapted protocol of TIPS at different thermal conditions (Table 1). Briefly,
 502 a POSS-terminated PUU polymer solution ^[56] was poured onto a square-shaped glass
 503 mold (100 mm × 100 mm × 500 μm in terms of width, length and height) and
 504 coagulated at different temperatures according to reference ^[43] to allow for solvent
 505 exchange, resulting in three different scaffold groups: CC (cryo-coagulation), CC+H
 506 (cryo-coagulation and heating), and RTC+H (room temperature coagulation and
 507 heating).

508 **Table 1 Processing conditions of TIPS**

Scaffolds	PUU-POSS solution poured on glass mold	Coagulation conditions	Thermal treatment
-----------	--	------------------------	-------------------

Room temperature coagulation + heating (RTC+H)	N/A	25°C water for 24 h	40°C water for 3 h
Cryo-coagulation (CC)	-20°C for 24 h	0°C ice water for 24 h	No thermal treatment
Cryo-coagulation +heating (CC+H)	-20°C for 24 h	0°C ice water for 24 h	40°C water for 3 h

509

510 **Characterization of dynamic stiffness:** Samples were subjected at wet condition to
511 mechanical tensile testing prior to and after incubation at 37°C during a 35-day period.
512 An Instron 5655 tester (USA) with a 1 mm/min rate and a 500 N cell load was used to
513 subject the samples (n=6) (250 mm length and 100 µm thickness) to static testing. A
514 5160 ElectroForce tester (USA) with 200 N load cells was used to subject the samples
515 (n=2) (10 mm length, 6.5 mm width and 2 mm thickness) to dynamic testing: 1 Hz
516 sinusoidal ramp, 25% tensile strain and up to 200,200 cycles.

517 **Characterization of the scaffold structure:** The morphology of the dried membranes
518 was examined under a Zeiss Supra 35VP FE-SEM microscope (Germany), and a
519 Poremaster 60GT porosimeter (UK) was used to evaluate the hierarchical porous
520 structure of freeze-dried membranes (n=2). A JEOL2100 FEG-TEM (Japan) and a
521 Bruker D8 Advance X-Ray diffractometer (Germany) were used to examine any phase
522 changes in the structure of the polymer prior to and after incubation at 37°C during a
523 28-day period.

524 **Wettability and protein adsorption:** Surface contact angle of the samples (n=20) was
525 characterized with a KRÜSS DSA 100 goniometer (Germany) based on a sessile drop
526 method using deionized water. A bicinchoninic acid (BCA) assay kit (Pierce, USA) was
527 used to evaluate protein adsorption on the membranes (n=3) using bovine serum
528 albumin (BSA) as standard in phosphate buffered saline (PBS), following reference [44];
529 membranes in serum free medium were used as blank. Tissue culture plate (TCP)
530 coverslips (Thermonax, USA) were used as control.

531 **Culture media and cell seeding:** Membranes (n=6) (11 mm diameter, 0.5 mm
532 thickness) were sterilized in ethanol (70% v/v) and seeded at a density of 5×10^4
533 cells/cm³ at second-passage (P2) with a human bone-marrow mesenchymal stem cell

534 line (hBM-MSCs) (Sciencell™, USA) in mesenchymal stem cell medium (MSCM)
535 (Sciencell™, USA). Media was replaced every three days.

536 **Metabolic activity and cellular proliferation:** The metabolic activity of cells was
537 monitored with alamarBlue® (Serotec Ltd., UK) testing (n=3), and cellular proliferation
538 with a fluorescent Hoechst 33258 stain over the course of 14 days (n=3). Cellular
539 morphology was observed at day 5 with a Zeiss Supra 35VP FE-SEM (Germany). TCP
540 was used as a non-stiffness softening and non-porous control.

541 **Cellular viability:** Cell viability was studied over the course of 10 days following
542 reference [43], with green FITC-labeled phalloidin (Life-technologies, UK) and blue
543 DAPI (Sigma-Aldrich, UK) staining against F-actin and cell nuclei respectively Images
544 were with x10 water objective lens using a Leica TCS SP8 confocal microscope
545 (Germany).

546 **Cellular differentiation:** Osteogenic and chondrogenic differentiation was induced with
547 supplemented osteogenic and chondrogenic differentiation media as detailed in
548 reference [44]. TCP and spheroid-derived MSCs were used, respectively, as 2D and 3D
549 positive controls of differentiation.

550 Static tensile testing of cell-laden membranes (n=6) was also performed after *in vitro*
551 differentiation as detailed above.

552 **Immunofluorescence staining:** Cell-laden membranes were collected after the
553 differentiation process. Immunofluorescent staining with markers against Collagen II
554 and Aggrecan (i.e. chondrogenesis), and markers against Collagen I and calcium (i.e.
555 osteogenesis), was carried out as detailed in reference [44]. F-actin was counterstained
556 with phalloidin Alexafluor®-488 (Sigma-Aldrich, UK). Images were taken with a Leica
557 TCS SP8vis confocal microscope.

558 **Measurement of sulfated glycosaminoglycans:** The amount of sGAG content in the
559 membranes (n=6) was quantified over a 4-week period with a Blyscan™ sulphated
560 glycosaminoglycan assay (Biocolor Ltd.; Antrim, UK), normalized to total DNA
561 levels.[43] The absorbance of dye-bound sGAG removed by centrifugation and
562 resuspended in dissociation reagent was read at 630 nm using a microplate reader
563 (Biotek; Swindon, UK), calculated using a standard curve obtained from
564 glycosaminoglycan standards provided with the kit.

565 **Measurement of extracellular calcium deposits:** To detect extracellular calcium
566 deposits in mineralization-positive cells, an alizarin Red staining assay (Sciencell™;
567 California, USA) was performed following the manufacturer's instructions. In brief,
568 cell-laden membranes (n=6) over a 21-day period of osteogenesis were fixed with 4 %
569 PFA in PBS, washed twice with diH₂O and stained with 1% Alizarin Red S (ARS, pH
570 4.2) for 20 min at room temperature. Excess stain was washed away with two changes
571 of diH₂O. Positive-stained cells were then destained with a 10% acetic acid solution for
572 30 min, followed by neutralization in ammonium hydroxide solution. The absorbance of
573 ARS extraction was measured at 520 nm with a microplate reader (Anthos 2020
574 microplate reader; Biochrome Ltd, UK).

575 Furthermore, a colorimetric Alkaline Phosphatase (ALP) assay kit (Merck Millipore,
576 USA) was used to determine ALP activity over a 3-week period (n=6). Briefly, culture
577 medium was removed by decantation and cells were washed with PBS and harvested in
578 1 mL universal ALP buffer. Cells were sonicated twice for 20 sec and centrifuged at
579 900×g for 5 min at 4°C. P-nitrophenyl phosphate substrate was added to the
580 supernatants and the reaction stopped with NaOH (100 µL, 0.1 N). The optical density
581 was measured at 405 nm using a microplate reader (Spectra Max Plus 384 MK3;
582 Thermo-Fisher, UK). The ALP activity was calculated from a standard curve after
583 normalization to total protein content, measured using the Bradford protein assay kit
584 (Pierce; Rockford IL, USA).

585 **Quantitative reverse transcriptase polymerase chain reaction (qPCR):**
586 Membranes (n=6) were analyzed by qRT-PCR using primers related to chondrogenesis
587 (*SOX9*, *COL2A1*, *COLX* and *ACAN*; **Table S7**) and osteogenesis (*ALP*, *COL1A1*,
588 *RUNX2*, *SPP1*, *BGLAP*, *SP7*; **Table S8**) as detailed in reference ^[44]. Relative gene
589 expression was normalized to GAPDH used as housekeeping gene.

590 **Enzyme-linked immunosorbent assay:** ELISA analysis (n=6) was used to detect
591 production of Aggrecan, Collagen II, glycosaminoglycans, Osteocalcin and Collagen I
592 as detailed in reference ^[44].

593 **Histological analysis:** Cell-laden membranes (n=2) fixed in 4% paraformaldehyde
594 (PFA) in PBS were embedded in paraffin and sectioned with a Leica RM2235 rotary
595 microtome. Gross cell morphology was studied with hematoxylin and eosin (H&E)
596 staining. Polysaccharide formation was evaluated with Alcian Blue (A-blue), with the

597 cell nuclei counterstained with nuclear fast red. Antibody collagen II (COL2) staining
598 was used to indicate collagen II production, calcium deposition was evaluated with
599 Alizarin Red S (ARS), and antibody collagen I (COL1) was used to stain against
600 collagen I production. Acellular membranes were used as negative control to account
601 for any false-positive signal.

602 ***Energy Dispersive X-Ray Spectroscopy:*** elemental surface composition of the
603 membranes (n=6) was evaluated with an EDX detector attached to a CrossBeam XB
604 1540 FIB-SEM microscope (Germany).

605 ***Statistical analysis:*** All results were presented as standard deviation (SD, error bars) of
606 the mean values, and performed at least in triplicate. Statistical analysis of the results
607 was carried out using GraphPad Prism 6 (San Diego, USA). The differences between
608 more than two groups were analyzed by two-way analysis of variance (ANOVA) (when
609 involving two independent variables), with Tukey's post hoc test. For comparing
610 parametric data between two groups, two-tailed unpaired Student's t-test was used. A
611 value of $p < 0.05$ was considered statistically significant.

612 **Acknowledgments**

613 The authors acknowledge financial support by the Engineering and Physical Sciences
614 Research Council in the United Kingdom (EPSRC grants Nos. EP/L020904/1,
615 EP/M026884/1 and EP/R02961X/1).

616 **Competing interests**

617 The authors declare no potential conflict of interests with respect to the research,
618 authorship and/or publication of this article.

619

620 **References**

- 621 [1] E. R. Ruskowitz, C. A. DeForest, *Nat. Rev. Mater.* **2018**, *3*, 17087.
622 [2] M. Guvendiren, J. A. Burdick, *Nat. Commun.* **2012**, *3*, 792.
623 [3] C. A. Engh, J. D. Boby, A. H. Glassman, *J. Bone Joint Surg. Br.* **1987**, *69*, 45.
624 [4] B. Hinz, *J. Invest. Dermatol.* **2007**, *127*, 526.
625 [5] G. Li, L. Wang, W. Pan, F. Yang, W. Jiang, X. Wu, X. Kong, K. Dai, Y. Hao, *Sci.*
626 *Rep.* **2016**, *6*, 34072.
627 [6] S. B. Mirza, D. G. Dunlop, S. S. Panesar, S. G. Naqvi, S. Gangoo, S. Salih, *Open*
628 *Orthop. J.* **2010**, *4*, 169.
629 [7] L. Shi, L. Shi, L. Wang, Y. Duan, W. Lei, Z. Wang, J. Li, X. Fan, X. Li, S. Li,
630 Z. Guo, *PLOS ONE* **2013**, *8*, e55015.
631 [8] K. Uto, J. H. Tsui, C. A. DeForest, D.-H. Kim, *Prog. Polym. Sci.* **2017**, *65*, 53.
632 [9] A. S. Gladman, E. A. Matsumoto, R. G. Nuzzo, L. Mahadevan, J. A. Lewis, *Nat.*
633 *Mater.* **2016**, *15*, 413.
634 [10] K. M. Ferlin, M. E. Prendergast, M. L. Miller, B.-N. B. Nguyen, D. S. Kaplan, J. P.
635 Fisher, *Mol. Pharm.* **2014**, *11*, 2172.
636 [11] D. E. Disher, P. Janmey, Y. Wang, *Mater. Biol.* **2005**, *310*, 5.
637 [12] A. J. Engler, S. Sen, H. L. Sweeney, D. E. Discher, *Cell* **2006**, *126*, 677.
638 [13] J. H. Wen, L. G. Vincent, A. Fuhrmann, Y. S. Choi, K. C. Hribar, H. Taylor-Weiner,
639 S. Chen, A. J. Engler, *Nat. Mater.* **2014**, *advance on*, 1.
640 [14] J. Pelham, Robert J., Y.-L. Wang, *Proc. Natl. Acad. Sci. U. S. A.* **1997**, *94*, 13661.
641 [15] I. Hopp, A. Michelmores, L. E. Smith, D. E. Robinson, A. Bachhuka, A.
642 Mierczynska, K. Vasilev, *Biomaterials* **2013**, *34*, 5070.
643 [16] C. M. Lo, H. B. Wang, M. Dembo, Y. L. Wang, *Biophys. J.* **2000**, *79*, 144.
644 [17] D. S. Gray, J. Tien, C. S. Chen, *J. Biomed. Mater. Res. A* **2003**, *66A*, 605.
645 [18] A. A. Abdeen, J. Lee, N. A. Bharadwaj, R. H. Ewoldt, K. A. Kilian, *Adv. Healthc.*
646 *Mater.* **2016**, *5*, 2536.
647 [19] S. R. Caliari, M. Perepelyuk, E. M. Soulas, G. Y. Lee, R. G. Wells, J. A. Burdick,
648 *Integr. Biol. Quant. Biosci. Nano Macro* **2016**, *8*, 720.
649 [20] Y. Lei, D. V. Schaffer, *Proc. Natl. Acad. Sci.* **2013**, *110*, E5039.
650 [21] H. Y. Yoshikawa, F. F. Rossetti, S. Kaufmann, T. Kaindl, J. Madsen, U. Engel, A.
651 L. Lewis, S. P. Armes, M. Tanaka, *J. Am. Chem. Soc.* **2011**, *133*, 1367.
652 [22] J. L. Young, A. J. Engler, *Biomaterials* **2011**, *32*, 1002.
653 [23] C. Yang, M. W. Tibbitt, L. Basta, K. S. Anseth, *Nat. Mater.* **2014**, *13*, 645.
654 [24] B. M. Gillette, J. A. Jensen, M. Wang, J. Tchao, S. K. Sia, *Adv. Mater.* **2010**, *22*,
655 686.
656 [25] R. S. Stowers, S. C. Allen, L. J. Suggs, *Proc. Natl. Acad. Sci. U. S. A.* **2015**, *112*,
657 1953.
658 [26] F. X. Jiang, B. Yurke, R. S. Schloss, B. L. Firestein, N. A. Langrana, *Tissue Eng.*
659 *Part A* **2010**, *16*, 1873.
660 [27] D. C. Lin, B. Yurke, N. A. Langrana, *J. Mater. Res.* **2005**, *20*, 1456.
661 [28] D. C. Lin, B. Yurke, N. A. Langrana, *J. Biomech. Eng.* **2004**, *126*, 104.
662 [29] S. Kumar, *Nat. Mater.* **2014**, *13*, 918.
663 [30] E. H. Ahn, Y. Kim, Kshitiz, S. S. An, J. Afzal, S. Lee, M. Kwak, K.-Y. Suh, D.-H.
664 Kim, A. Levchenko, *Biomaterials* **2014**, *35*, 2401.
665 [31] J. Zeltinger, J. K. Sherwood, D. A. Graham, R. Mueller, L. G. Griffith, *Tissue Eng.*
666 **2001**, *7*, 557.
667 [32] A. K. Salem, R. Stevens, R. G. Pearson, M. C. Davies, S. J. B. Tendler, C. J.
668 Roberts, P. M. Williams, K. M. Shakesheff, *J. Biomed. Mater. Res.* **2002**, *61*, 212.

- 669 [33] C. M. Murphy, M. G. Haugh, F. J. O'Brien, *Biomaterials* **2010**, *31*, 461.
- 670 [34] E. M. Byrne, E. Farrell, L. A. McMahon, M. G. Haugh, F. J. O'Brien, V. A.
- 671 Campbell, P. J. Prendergast, B. C. O'Connell, *J. Mater. Sci. Mater. Med.* **2008**, *19*,
- 672 3455.
- 673 [35] F. J. O'Brien, B. A. Harley, M. A. Waller, I. V. Yannas, L. J. Gibson, P. J.
- 674 Prendergast, *Technol. Health Care Off. J. Eur. Soc. Eng. Med.* **2007**, *15*, 3.
- 675 [36] A. Matsiko, J. P. Gleeson, F. J. O'Brien, *Tissue Eng. Part A* **2014**, *21*, 486.
- 676 [37] H. Janik, M. Marzec, *Mater. Sci. Eng. C* **2015**, *48*, 586.
- 677 [38] F. Dehghani, N. Annabi, *Curr. Opin. Biotechnol.* **2011**, *22*, 661.
- 678 [39] J. D. Fromstein, K. A. Woodhouse, *J. Biomater. Sci. Polym. Ed.* **2002**, *13*, 391.
- 679 [40] L. Draghi, S. Resta, M. G. Pirozzolo, M. C. Tanzi, *J. Mater. Sci. Mater. Med.* **2005**,
- 680 *16*, 1093.
- 681 [41] J. Guan, K. L. Fujimoto, M. S. Sacks, W. R. Wagner, *Biomaterials* **2005**, *26*, 3961.
- 682 [42] R. Akbarzadeh, A.-M. Yousefi, *J. Biomed. Mater. Res. B Appl. Biomater.* **2014**,
- 683 *102*, 1304.
- 684 [43] L. Wu, J. Virdee, E. Maughan, A. Darbyshire, G. Jell, M. Loizidou, M. Emberton,
- 685 P. Butler, A. Howkins, A. Reynolds, I. Boyd, M. Birchall, W. Song, *Acta Biomater.*
- 686 **2018**, *80*, 188.
- 687 [44] L. Wu, A. Magaz, T. Wang, C. Liu, A. Darbyshire, M. Loizidou, M. Emberton, M.
- 688 Birchall, W. Song, *Biomaterials* **2018**, *186*, 64.
- 689 [45] L. Wu, A. Magaz, E. Maughan, N. Oliver, A. Darbyshire, M. Loizidou, M.
- 690 Emberton, M. Birchall, W. Song, *Acta Biomater.* **2019**, *86*, 157.
- 691 [46] N. Wang, K. Burugapalli, W. Song, J. Halls, F. Moussy, Y. Zheng, Y. Ma, Z. Wu,
- 692 K. Li, *J. Membr. Sci.* **2013**, *427*, 207.
- 693 [47] T. E. Hardingham, R. A. Oldershaw, S. R. Tew, *J. Anat.* **2006**, *209*, 469.
- 694 [48] H. D. Kim, Y. Lee, Y. Kim, Y. Hwang, N. S. Hwang, *Polymers* **2017**, *9*, 655.
- 695 [49] P. A. Levett, D. W. Hutmacher, J. Malda, T. J. Klein, *PLoS ONE* **2014**, *9*, DOI
- 696 10.1371/journal.pone.0113216.
- 697 [50] K. L. Moffat, W.-H. S. Sun, N. O. Chahine, P. E. Pena, S. B. Doty, C. T. Hung, G.
- 698 A. Ateshian, H. H. Lu, *Conf. Proc. Annu. Int. Conf. IEEE Eng. Med. Biol. Soc.*
- 699 *IEEE Eng. Med. Biol. Soc. Annu. Conf.* **2006**, *1*, 2366.
- 700 [51] K. A. Athanasiou, M. P. Rosenwasser, J. A. Buckwalter, T. I. Malinin, V. C. Mow,
- 701 *J. Orthop. Res. Off. Publ. Orthop. Res. Soc.* **1991**, *9*, 330.
- 702 [52] K. A. Athanasiou, A. Agarwal, F. J. Dzida, *J. Orthop. Res. Off. Publ. Orthop. Res.*
- 703 *Soc.* **1994**, *12*, 340.
- 704 [53] L. Zhang, J. Hu, K. A. Athanasiou, *Crit. Rev. Biomed. Eng.* **2009**, *37*, 1.
- 705 [54] M. F. Griffin, Y. Premakumar, A. M. Seifalian, M. Szarko, P. E. M. Butler, *Ann.*
- 706 *Biomed. Eng.* **2016**, *44*, 3460.
- 707 [55] Y.-R. V. Shih, K.-F. Tseng, H.-Y. Lai, C.-H. Lin, O. K. Lee, *J. Bone Miner. Res.*
- 708 *Off. J. Am. Soc. Bone Miner. Res.* **2011**, *26*, 730.
- 709 [56] R. Y. Kannan, H. J. Salacinski, M. Odlyha, P. E. Butler, A. M. Seifalian,
- 710 *Biomaterials* **2006**, *27*, 1971.
- 711
- 712
- 713
- 714

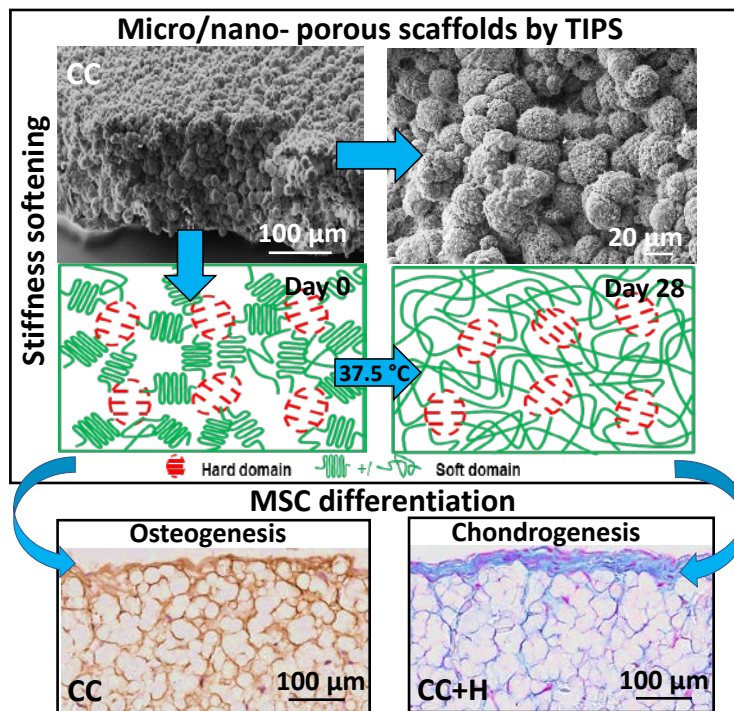
715

716 **Table of Contents (ToC)**

717 **ToC summary:**

718 **Elastomeric nanohybrid membranes with thermoresponsive stiffness softening and**
719 **unique porous structure** were developed by thermally-induced phase separation
720 (TIPS). The initial stiffness and subsequent stiffness softening coupled with the
721 interconnected micro/nano- porous structure of the membranes promote niches that
722 regulate the differentiation of human bone-marrow derived mesenchymal stem cells
723 towards the osteogenic and chondrogenic lineages, promising smart scaffolds/coatings
724 with matched mechanical properties for tissue reconstruction and regeneration.

725 **ToC figure:**



726

727 **ToC keyword:**

728 Stiffness softening, stem cell chondrogenesis, osteogenesis, elastomer nanohybrid, TIPS
729 porous membrane

730

731

732

733

734

735 **Supporting data**

736 **Table S1** Physico-mechanical properties of stiffness softening porous membranes,
 737 before and after relaxation at body temperature (n=6).

3D-TIPS scaffold		Scaffold Density, kg.m ⁻³	Total Porosity, 100%	Tensile modulus @50% strain, MPa	Tensile modulus @100% strain, MPa	Ultimate Strength, MPa	Strain at break, %	Toughness, J. m ⁻³ × 10 ⁴
CC	D0	41 (±3)	89 (±2)	20.0 (±1.9)	19.8(±2)	20.7(±0.4)	711 (±30)	767 (±29)
	D28	60 (±3)	83 (±2)	7.7(±1.7)	7.2(±1.9)	3.7 (±1.1)	433 (±35)	402(±70)
	D35	63 (±7)	84(±7)	3(±1.7)	2.9(±1.9)	2.2 (±1.2)	318 (±67)	332 (±67)
CC+H	D0	68 (±5)	80 (±2)	7.3 (±0.9)	7.1 (±1)	5.7(±0.3)	496 (±32)	492 (±32)
	D28	73(±8)	79(±2)	5.8 (±0.4)	4.3 (±0.8)	2.7 (±0.4)	398(±41)	311(±51)
	D35	75 (±9)	78 (±4)	2.6 (±0.5)	2.9(±0.7)	2.10(±0.5)	319 (±42)	321(±51)
RTC+H	D0	90 (±12)	71(±2)	2.1(±0.2)	2.2 (±0.5)	2.2 (±0.2)	295(±25)	295 (±25)
	D28	92(±10)	70(±1)	2.1 (±0.7)	2.2 (±0.4)	2.1 (±0.6)	287 (±31)	308(±33)
	D35	92 (±9)	71 (±3)	2.2 (±0.4)	2.1 (±0.4)	1.9 (±0.3)	298 (±32)	318 (±31)

738

739

740

741

742

743

744

745

746 **Table S2** Hysteresis values (i.e. energy lost) of the various membranes before and after
 747 thermal relaxation during tensile cyclic loading in the strain domain (n=2).

Type of test	Day	No. of cycles	Hysteresis energy (J.m ⁻³)		
			CC	CC+H	RTC+H
Tensile	D0	0-200	147 (±21)	35 (±9)	10(±1)
		10,000-10,200	63(±8)	20 (±3)	8(±3)
		100,000-10,200	41(±10)	15 (±3)	5(±3)
		200,000-200,200	19 (±4)	7(±4)	4(±3)
	D28	0-200	28 (±4)	18(±3)	9(±3)
		10,000-10,200	20(±5)	12(±3)	8(±2)
		100,000-10,200	12(±3)	10 (±3)	5(±3)
		200,000-200,200	9 (±4)	10(±2)	5(±1)
	D35	0-200	5.1(±1)	5 (±1)	5.3(±1)
		10,000-10,200	4.2(±1)	4.7 (±1)	4.3 (±1)
		100,000-10,200	4.2(±0.9)	4.1(±1)	4.11 (±1)
		200,000-200,200	4.4(±0.4)	4.3(±0.7)	4.09 (±1)

748

749

750

751

752

753

754

755

756

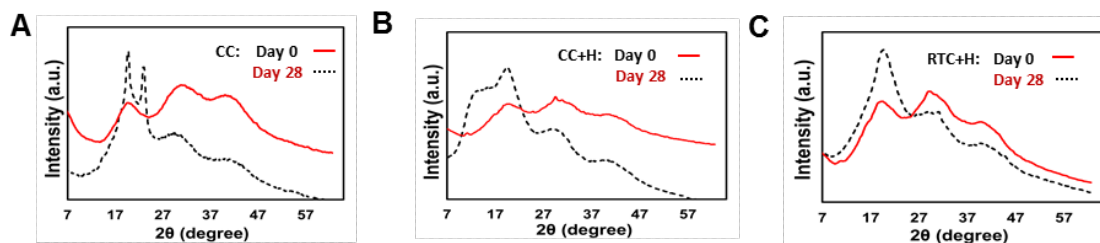
757

758 **Table S3** Pore diameter, pore volume and relative pore surface fraction of stiffness
 759 softening porous membranes at day 0 and after 28 days at body temperature *in vitro*.

TIPS scaffold		Pore Diameter, nm	Pore Volume, cm ³ .g ⁻¹	Relative Pore Volume, %	Surface Area, m ² .g ⁻¹	Relative Surface Area, %
Day 0	CC	1000,000 to 10,000	13.4	16	25.7	16
		10,000 to 37	32.1	38	101.2	63
		37 to 5	39.6	46	34	21
		Total		85.3		160.9
	CC+H	1000,000 to 10,000	11.8	20	23.7	18
		10,000 to 37	28.6	31	79.2	62
		37 to 5	18.5	49	25.3	20
		Total		58.9		128.2
	RTC+H	1000,000 to 10,000	15.9	51	28.9	58
		10,000 to 37	0.1	0.3	4	8
		37 to 5	14.6	48.7	17	34
		Total		30.6		49.9
Day 28	CC	1000,000 to 10,000	12.6	16	25.6	16
		10,000 to 37	32.1	40	96.2	62
		37 to 5	35.1	44	34	22
		Total		79.7		155.8
	CC+H	350,000 to 10,000	11.2	20	22	18
		10,000 to 37	28.1	50	74.9	62
		37 to 5	17.1	30	23.2	20
		Total		56.4		120.1
	RTC+H	350,000 to 10,000	14.2	49	26.9	55
		10,000 to 37	0.2	0.7	5.4	11

		37 to 5	14.4	50.3	17	34
	Total		28.8		49.2	

760



761

762 **Figure S1** XRD spectra of the membranes showing ‘stiffness memory’ after *in vitro*
 763 incubation at 37°C.

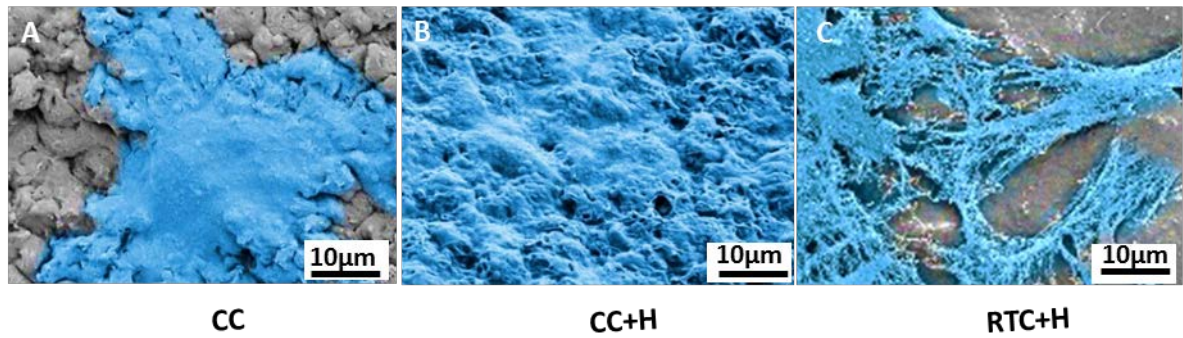
764

765 **Table S4** Evolution of XRD peaks of the membranes with ‘stiffness memory’ over 28
 766 days *in vitro* incubation. Degree of crystallinity (Dc, %), d-spacing (d, Å)

Membranes		Day 0			Day 28		
		2θ	d	Dc	2θ	d	Dc
CC	Sharp peak 1	20.02	4.43	37.6			
	Sharp peak 2	23.19	3.83				
	Broad halo peak 1						
	Broad halo peak 2				20.18		
	Broad halo peak 3				31.25		
	Broad halo peak 4				41.92		
CC+H	Sharp peak 1						
	Sharp peak 2						
	Broad halo peak 1	12.22					
	Broad halo peak 2	23.19			19.96		
	Broad halo peak 3	30.13			30.86		
	Broad halo peak 4	41.29			41.92		
RTC+H	Sharp peak 1						
	Sharp peak 2						
	Broad halo peak 1						
	Broad halo peak 2	20.18			21.23		
	Broad halo peak 3	30.13			30.72		
	Broad halo peak 4	41.29			42.76		

767

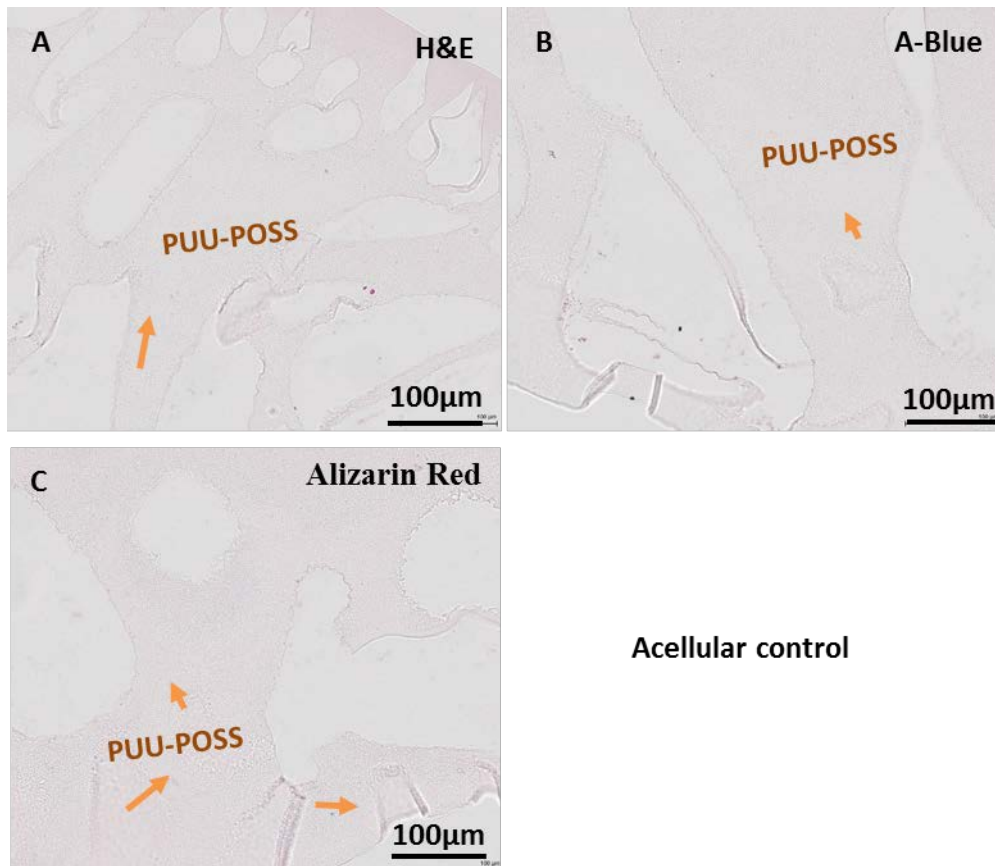
Day 5



768

769 **Figure S2 Cellular morphology at day 5 as observed by SEM: (A) CC, (B) CC+H**
770 **and (C) RTC+H scaffolds.**

771



772

773 **Figure S3 (A-C) Non cell-laden membranes used as negative control during**
774 **histological staining with Hematoxylin and Eosin, Alcian Blue and Alizarin Red.**

775

776

777 **Table S5** EDX element analysis of membranes after day 28 chondrogenesis (n=6)

Element	CC		CC+H		RTC+H	
	Wt %	At %	Wt %	At %	Wt %	At %
C	59.6(±10)	72.9(±11)	69.3(±13)	84(±20)	70.5(±19)	84.6(±19)
O	22.7(±4)	21.1(±5)	15.6(±5)	14(±4)	16.4(±5)	14.7(±6)
Na	3.5(±1)	2.3(±1)	0.6(±0.2)	0.4(±0.1)	0.7(±0.2)	0.4(±0.1)
Si	5.4(±2)	2.9(±1)	0.3(±0.1)	0.2(±0.1)	0.7(±0.1)	0.4(±0.1)
P	0.4(±0.1)	0.2(±0.1)	0.2(±0.1)	0.2(±0.1)	0.3(±0.1)	0.1(±0.04)
Ca	0.1(±0.03)	0.1(±0.02)	0.2(±0.1)	0.1(±0.01)	0.1(±0.03)	0.1(±0.02)
Au	8.4(±2)	0.6(±0.3)	13.7(±4)	1.0(±0.3)	11.4(±3)	0.8(±0.3)
Total	100%	100%	100%	100%	100%	100%

778

779

780 **Table S6** EDX element analysis of the membranes after 21 days osteogenesis (n=6)

Element	CC		CC+H		RTC+H	
	Wt %	At %	Wt %	At %	Wt %	At %
C	80.1(±19)	90.6(±18)	69(±17)	76.9(±22)	65.6(±17)	80 (±17)
O	7.2(±2)	6(±2)	20.2(±6)	20(±6)	19.6(±5)	18.4(±2)
Na	2.6(±1)	0.9(±0.2)	1(±0.3)	1.1(±0.3)	0.5(±0.2)	0.3(±0.1)
Si	1.1(±0.5)	0.8(±0.2)	0.4(±0.1)	0.6(±0.1)	0.2(±0.04)	0.1(±0.02)
P	0.6(±0.1)	0.5(±0.1)	0.2(±0.07)	0.2(±0.1)	0.1(±0.02)	0.1(±0.03)
Ca	2.9(±1)	0.9(±0.2)	0.9(±0.2)	0.6(±0.2)	0.1(±0.02)	0.1(±0.03)
Au	5.5(±1)	0.3(±0.05)	8.4(±2)	0.7(±0.2)	13.8(±3)	1.1(±0.3)
Total	100%	100%	100%	100%	100%	100%

781

782

783 **Supporting methodology**

784 **Table S7** List of primers used for qPCR (chondrogenesis)

Gene	Primer sequence (sense/antisense)	Tm (°C)
<i>SOX9</i>	5'-GCCTTTTTGTCCATCCCTTTTTTC-3'	64.6
	5'-GTCCTTGGGGTTCTTGCTGATGTA-3'	65.3
<i>COL2A1</i>	5'-ACCTCACGCCTCCCCATCATTG-3'	62.0
	5'-ACATCAGGTCAGGTCAGCCATTCAG-3'	62.6
<i>COLX</i>	5'-TGAAAGGGACTCATGTTTGGGTAGG-3'	60.5
	5'-ACTCACATTGGAGCCACTAGGAATC-3'	60.4
<i>ACCAN</i>	5'-TGAGGAGGGCTGGAACAAGTACC-3'	61.0
	5'-GGAGGTGCTAATTGCAGGGAACA-3'	62.3
<i>GAPDH</i>	5'-TGATGACATCAAGAAGGTGGTGAAG-3'	60.0
	5'-TCCTTGGAGGCCATGTGGGCCAT-3'	60.0

785 *SOX9*, transcription factor *SOX9*; *COL2A1*, collagen type II; *COLX*, collagen type X;
 786 *ACAN*, Aggrecan; *GAPDH*, glyceraldehyde phosphate dehydrogenase.

787

788

789

790

791

792

793

794

795

796

797

798

799 **Table S8** List of primers used for qPCR (osteogenesis)

Gene	Primer sequence (sense/antisense)	Tm (°C)
<i>ALP</i>	5'-GCCTTTTTGTCCATCCCTTTTTTC-3'	64.6
	5'-GTCCTTGGGGTTCTTGCTGATGTA-3'	65.3
<i>COL1A1</i>	5'-CGCTACTACCGGGCTGATGAT-3'	62.0
	5'-GTCCTTGGGGTTCTTGCTGATGTA-3'	62.6
<i>RUNX2</i>	5'-AGAGGTACCAGATGGGACTGTGGTT-3'	61.76
	5'-GGTAGCTACTTGGGGAGGATTTGTG-3'	62.63
<i>SPPI</i>	5'-ACTTGGAAGGGTCTGTGGGGCT-3'	60.5
	5'-AGGCATCACCTGTGCCATACCA-3'	60.4
<i>BGLAP</i>	5'-ATGAGAGCCCTCACACTCCTC-3'	61.0
	5'-GCCGTAGAAGCCGATAGGC-3'	62.3
<i>SP7</i>	5'-TGCACTCTCCCTGCCAGACCTC-3'	60.0
	5'-AACGGGTCCCAAGGAGCCAGG-3'	60.0
<i>GAPDH</i>	5'-TGATGACATCAAGAAGGTGGTGAAG-3'	60.0
	5'-TCCTTGGAGGCCATGTGGGCCAT-3'	60.0

800 *ALP*, alkaline phosphatase; *COL1A1*, collagen type I; *RUNX2*, cbfa-1; *SPPI*,
801 Osteopontin; *BGLAP*, Osteocalcin; *SP7*, Osterix; *GAPDH*, glyceraldehyde phosphate
802 dehydrogenase.

803